# Adaptive Linear Time-Varying Parameter-Varying Modeling of Lithium-Ion Batteries Considering Aging Phenomenon

Jie Hou, *Member, IEEE*, Yuchao Jiang, Jingxiang Liu, *Member, IEEE*, Penghua Li, *Member, IEEE*, Sheng Xiang, *Member, IEEE*, Liping Chen, *Member, IEEE*, and Zhongwei Deng, *Senior Member, IEEE*

***Abstract*—Achieving a balance between accuracy and complexity remains a significant challenge for lithium batteries. The accuracy of the model is usually positively correlated with the complexity of the model. A simple model cannot capture more influencing factors, as simpler models often fail to capture the full range of influencing factors. This article presents an enhanced battery model that extends the traditional equivalent circuit model (ECM) by integrating a set of exogenous independent parameters, encompassing both internal and external battery characteristics, into the system matrix via a polynomial relationship. This results in a time-varying system matrix that allows for a comprehensive representation of battery parameters and effective data fusion while simplifying the model. The model also addresses aging and other time-varying phenomena through time-varying exogenous functions, thus simplifying the management of aging effects. Recursive least squares algorithms with an adaptive forgetting factor handle time-varying parameters and aging effects, ensuring rapid adaptation to data changes while preserving high performance and accuracy. Through simulation and aging battery experiments, the mean absolute error and root mean square error of the proposed scheme can be controlled within 13.6 and 16.0 mV, which proves its accuracy and superiority, and has great potential in aging battery applications.**

***Index Terms*—Adaptive modeling method, linear parameter-varying model, lithium-ion battery.**

## I. Introduction

Lithium batteries are widely used in electric vehicles and industrial systems due to their superior properties, including long lifespan, high energy density, low self-discharge rate, etc. [1], [2]. These applications, which are safe, reliable, and efficient in operation, usually require the support of battery management systems (BMSs) [3], [4], and efficient BMS cannot be separated from accurate battery models [5].

Therefore, various battery models have been proposed, which are mainly categorized into neural network models [6], electrochemical models (EM) [7], and equivalent circuit models (ECM) [8]. The neural network model does not need to consider the internal feature changes [9], but its training process is complex and difficult to apply online [10]. EM can use partial differential equations to express the diffusion and migration process inside the battery, so it requires a lot of effort to parameterize the micro-parameters and deal with their computational load, which is unsuitable for real-time applications [11]. ECM can describe battery behavior with only a few circuit elements, but can only reflect some external characteristics of the battery and ignore internal chemical processes [12], making it an ideal battery model for online applications [13].

Numerous studies have shown that the accuracy of a battery model is positively correlated with its complexity [14]. However, as in the case of the models presented above, most battery modeling methods require a tradeoff between model complexity and accuracy during design [15], [16]. Therefore, many researchers have been devoted to seeking such a balanced "bridge" in control-oriented battery modeling [17], [18].

Fortunately, the ECM demonstrates a simple structure and ease of computation in the aforementioned modeling approach [19], therefore, it is an appropriate model for the extension to enhance its accuracy. Currently, the expansion methods for ECM are roughly divided into two types: adding the external circuit module and extending the internal state. The methods of adding the external circuit module include adding temperature dependence to the ECM and combining it with set-affiliation techniques [20]. The Wiener model was added to the ECM to give it the ability to capture nonlinear properties [10]. In [21], a 2-D grid long short-term memory model was incorporated into the ECM. Li et al. [12] combined long and short-term neural networks with ECM. The improved ECM model [22]

Received 17 January 2025; revised 18 April 2025 and 3 June 2025; accepted 6 July 2025. Date of publication 11 July 2025; date of current version 27 August 2025. This work was supported in part by National Natural Science Foundation of China under Grant 62373070, Grant 52272388, Grant 61903057, Grant 52472401, in part by China's National Key Program under Grant 2025YFE0103000, in part by Chongqing Natural Science Foundation under Grant CSTB2024NSCQ-QCXMX0054, Grant CSTB2022NSCQ-MSX1225,cstc2024ycjh-bgzxm0042, in part by the Natural Science Foundation of Liaoning province under Grant 2024-BS-017, in part by the Key research and development project of Anhui Province under Grant 202304a05020060, in part by Sichuan Science and Technology Program under Grant 2024NSFSC0938, and in part by Anhui Provincial Natural Science Outstanding Youth Foundation under Grant 2408085J038. Recommended for publication by Associate Editor H. Chaoui. *(Corresponding author: Jie Hou.)*

Jie Hou, Yuchao Jiang, Penghua Li, and Sheng Xiang are with the Chongqing University of Posts and Telecommunications, Chongqing, 400065, China (e-mail: houjie@cqupt.edu.cn, jiehou.phd@hotmail.com).

Jingxiang Liu is with the School of Marine Electrical Engineering, Dalian Maritime University, Dalian 116026, China.

Liping Chen is with the School of Electrical Engineering and Automation, Hefei University of Technology, Hefei 230009, China.

Zhongwei Deng is with the School of Mechanical and Electrical Engineering, University of Electronic Science and Technology of China, Chengdu 611731, China.

Color versions of one or more figures in this article are available at https://doi.org/10.1109/TPEL.2025.3588296.

Digital Object Identifier 10.1109/TPEL.2025.3588296

reduces the end-voltage estimation error. In [23], a nonlinear over-voltage model was added to improve voltage accuracy for dynamic battery conditions at low temperatures. However, the methods of adding extra modules to the external circuit may introduce unnecessary noise interference, power loss, and other errors. Another method is to extend the internal state method, such as those in [24], which incorporated the battery state of charge (SOC) within the estimator. Wang et al. [25] proposed that the state of energy in a battery is a measure of its nonlinear behavior. Zhang et al. [26] introduced a nonlinear extended state observer that compensates for the total disturbances in the battery. However, these extended ECM modeling approaches still have limitations, they only consider the influence of a single factor and cannot use a general model to fully characterize all the internal changes and external characteristics of lithium batteries.

From the abovementioned discussion, it is clear that in the precise modeling of lithium batteries, a major challenge is how to use a single model to simultaneously represent both the internal reactions and external characteristics that affect battery performance. It should first be able to describe the battery's complex nonlinear characteristics simply. Second, it should have online foundational algorithms and general frameworks for identification procedures, making it accessible to the general public. Therefore, this article proposes a Linear Time-Varying Parameter-Varying (LTPV) model, aiming to achieve all the aforementioned goals and challenges, while striking a balance between the accuracy and complexity of the battery model. The main novelties are as follows.

1) An extended ECM in simple linear form, through a polynomial relationship to characterize both internal and external factors of lithium batteries is proposed. This not only provides a broad scope for studying the influencing factors of lithium-ion battery performance, but also alleviates the difficulty and complexity of modeling and parameter calculation that arise from an excessive number of modeling conditions. The model retains the advantages of the ECM while addressing its shortcomings in capturing internal mechanistic responses and external characteristics. The model architecture achieves more accurate voltage prediction compared to traditional ECM and its identification methods.
2) An online identification framework with an adaptive forgetting factor, incorporating three recursive least squares algorithms, is proposed to identify the extended ECM. By stacking, iterating, and reconstructing matrices containing nonlinear factors, the model's output is linearly related to the input behavior, and the effects of aging and degradation of lithium batteries are reflected by time-varying parameters. Thus, the proposed identification framework can address the effects of nonlinearity, aging, and degradation of lithium batteries with good stability and tracking capabilities in a simplified way, thus improving the model's accuracy.

The rest of this article is organized as follows. Section II presents the new modeling framework. Section III proposes an online adapted algorithm. Section IV provides simulation examples and Section V provides real datasets to validate the merits of the proposed method. Finally, Section VI concludes this article.

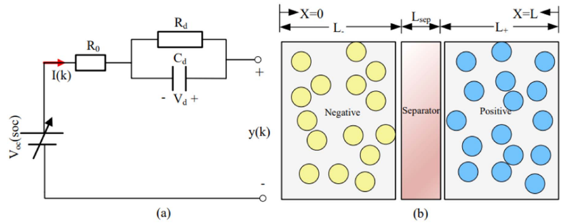

Fig. 1. (a) First-order ECM for battery. (b) Schematic of battery.

## II. LITHIUM-ION BATTERY LTVP MODELING

A simple, low-order, low-nonlinearity model architecture, namely, a linear parameter-varying model, is proposed to integrate data for lithium-ion batteries with nonlinear and time-varying characteristics. This model extends the linearized ECM.

### A. Analysis of ECMs

The ECM of a lithium battery is a linear representation that simplifies the intricate battery behavior by utilizing a diverse array of circuit elements arranged in series and parallel configurations to mimic the battery's external characteristics, which involves fewer parameters, entails simpler calculations, and is, therefore, more widely adopted. A generalized form of an ECM is given as follows:

$$\begin{cases} x(k+1) = Ax(k) + Bu(k) + w(k) \\ y(k) = Cx(k) + Du(k) + v(k) \end{cases} \tag{1}$$

where the system input $u(k)$ is the current of the battery, the system output $y(k)$ is the output voltage of the battery, the state vector $x(k) \in \mathbb{R}^{n_x}$ denotes the voltage drop, and SOC of the RC network in a lithium battery, where system order $n_x$ is usually set to 2 or 3, corresponding to the first-order and second-order ECMs. $w(k)$ and $v(k)$ denote model uncertainties and data uncertainties like noise errors, and unmodeled dynamics behaviors, respectively. Taking the first-order ECM as an example, the corresponding structure diagrams are shown in Fig. 1(a), and the detailed values of system matrices can be expressed in the following form:

$$A = \begin{bmatrix} 1 & 0 \\ 0 & e^{-\frac{T_s}{R_d C_d}} \end{bmatrix}, \quad B = \begin{bmatrix} \frac{T_s}{C_s} \\ R_d \cdot e^{-\frac{T_s}{R_d C_d}} \end{bmatrix},$$
$$C = \begin{bmatrix} \frac{\partial f(\text{soc})}{\partial \text{soc}} & 1 \end{bmatrix}, \quad D = R_0 \tag{2}$$

where $R_d, C_d$ form an RC network, $R_0$ is an ohmic resistor, $T_s$ is the sampling time, $C_n$ is the capacity of the battery, and $f(\text{soc})$ is the open-circuit voltage, which is a slowly time-varying nonlinear function concerning SOC.

The ECM model is a simple structure with fewer parameters. Even if more RC networks are included in the system matrix, the accuracy of the model is not significantly improved. Therefore, the ECM is regarded as a low-order and linear model structure, suitable for onboard implementation. However, ECM still has two limitations as follows.

1) Equivalent circuit simplification ignores the intricate dynamic variations and mechanistic processes that occur both within and outside the lithium battery, which fails to fully capture all factors that influence the performance of lithium batteries. Under complex operating conditions, the precision and accuracy of the ECM may be insufficient to meet stringent control requirements.
2) Equivalent circuits are linear approximations of battery behavior. However, a single linear model cannot predict the full range of nonlinear behaviors exhibited by batteries, thereby limiting the robustness and utility of ECM for industrial applications.

To retain the advantages of the ECM model while addressing its disadvantages, we have developed a new enhanced ECM model, specifically focusing on the system matrices.

### B. The Proposed LTPV Model

The system matrix $A$ describes dynamic changes in the internal state of the battery, influenced by factors such as internal chemical reactions, charging and discharging rates, temperature changes, battery aging, and degradation. The system matrix $B$ describes how external inputs impact the internal state, including external load changes, charging strategies, discharging strategies, and operation modes [27]. The system matrix $C$ defines the relationship between the battery output and state variables, which are influenced by the battery's state, operating conditions, structure, and materials. The system matrix $D$ describes the direct influence of inputs on outputs. Therefore, $C$ and $D$ generally remain unchanged under steady-state operating conditions of the selected cells.

The matrices $A$ and $B$ are affected by many influencing factors, integrate these factors into a single scheduling matrix $\mu(k)$ to visualize their roles and maintain the simplicity of the model (1)

$$A(\mu(k)) = A(\text{soc}(k), T(k), i_d(k), \ldots) \tag{3}$$

$$B(\mu(k)) = B(\text{soc}(k), T(k), i_d(k), \ldots) \tag{4}$$

where $\mu(k)$ represents all influences affecting the system matrices, such as SOC, temperature ($T$), and current direction ($i_d$) of the battery. The symbol "..." indicates that $\mu(k)$ can include additional variables not mentioned above but relevant to the battery's performance. By introducing $\mu(k)$, can consolidate all variables involved in the system matrix function into a single matrix, thereby simplifying the model's structure.

Next, examine the specific forms of $A(\mu(k))$ and $B(\mu(k))$ for practical online use. Since the precise effects of these influences on the system matrix are often unknown and may exhibit nonlinear relationships [28], the forms of $A(\mu(k))$ and $B(\mu(k))$ should be flexible and adaptable to the actual situation and the control system's design complexity.

Nonlinear physical chemistry processes significantly affect battery system behavior, creating a nonlinear dependence of the system matrix on these factors. Given that these nonlinear processes may smooth over short time scales, a nonlinear polynomial dependence can be used to represent the relationship between the system matrix and influencing factors [29]

$$\begin{aligned} A(\mu(k)) &= \mu^{(1)}(k)A^{(1)}(k) + \cdots + \mu^{(m)}(k)A^{(m)}(k) \\ &= \sum_{i=1}^{m} \mu^{(i)}(k)A^{(i)} \end{aligned} \tag{5}$$

$$\begin{aligned} B(\mu(k)) &= \mu^{(1)}(k)B^{(1)}(k) + \cdots + \mu^{(m)}(k)B^{(m)}(k) \\ &= \sum_{i=1}^{m} \mu^{(i)}(k)B^{(i)} \end{aligned} \tag{6}$$

where $\mu^{(i)}$ is the $i$th scheduling variable and $m$ is the number of influencing factors in the scheduling matrix. The system matrices $A^{(i)}$ and $B^{(i)}$ represent constants for a fixed $\mu^{(i)}$.

Note that the polynomial-dependent forms of (5) and (6) are linear functions of the known polynomial nonlinear terms $\mu^{(i)}$. This approach not only ensures simplicity in the parameter dependence and ease of computation, but also preserves the model's nonlinearity.

Combining (5), (6), and (1), we get follows LTPV model:

$$\begin{cases} x(k+1) = A(\mu(k))x(k) + B(\mu(k))u(k) + w(k) \\ = \sum_{i=1}^{m} \mu^{(i)}(k)\left(A^{(i)}x(k) + B^{(i)}u(k)\right) + w(k) \\ y(k) = Cx(k) + Du(k) + v(k) \end{cases} \tag{7}$$

where the polynomial functions $A(\mu(k))$ and $B(\mu(k))$ integrate all internal and external factors affecting lithium battery performance via $\mu(k)$. Refer to these as time-varying system matrices. The remaining notation is defined similarly to (1). The proposed LTPV model features a simpler structure, requiring no additional modules or preprocessing of battery data. A single scheduling matrix effectively captures the complex dynamics and nonlinear characteristics of lithium batteries. Note that the proposed model (7) can be directly extended to any other arbitrary model order, based on the number of RC branches selected for the ECM at the beginning.

The goal of this article is to identify the system parameters $A^{(i)}$, $B^{(i)}$, $C$, and $D$ based on the obtained data, including $u(k)$, $y(k)$, and $\mu(k)$.

*Remark 1:* The $\mu(k)$ is a time-varying vector that can combine multiple dynamical trajectories and be adjusted according to changes in lithium battery dynamics to achieve satisfactory model performance. For a given trajectory, where parameter variation depends on time, the LTPV system becomes a linear time-varying system. For a constant trajectory, where the scheduling variable is fixed, the LTPV system becomes a linear time-invariant system, with model (1) as a typical example. By determining the form and range of parameter dependencies in LTPV systems, appropriate lithium battery LTPV systems can be defined for various complex environments. In this article, the linear component of the scheduling matrix is SOC. Specifically set the nonlinear component of the scheduling variable as a second-order polynomial function of SOC, enabling smoother characterization of the battery's nonlinear characteristics [29], [30].

*Remark 2:* The impacts of various internal and external factors on matrices $A$ and $B$ are often difficult to express specifically and measure directly, requiring inference from other measurements or estimation through certain methods. Therefore, this study employs SOC as a comprehensive representation of these internal and external factors to indirectly reflect the influence of temperature variations, hysteresis effects, and diffusion phenomena on battery performance, especially aging degradation. Physically, SOC represents the quantity of remaining active materials within the battery, indicating the potential concentration of lithium ions available for power delivery. It serves as an integrated characterization of the nonlinear dynamic behavior of lithium-ion batteries. Importantly, SOC can be directly calculated from current and voltage measurements, making it a more readily obtainable influencing factor. The detailed expression of the abovementioned factors will form the research pathways for our future work.

## III. Adaptive Recursive Predictor-Based Subspace Identification

This section proposes an adaptive recursive identification algorithm that utilizes three linear regression techniques to identify the LTPV model from measurement data.

### A. Input–Output Relationship Reconstruction

To eliminate the detrimental effects of noise on the identification results, use the Kalman filtering principle to represent the model (7) in the following innovation form:

$$\begin{cases} x(k+1)=\sum_{i=1}^{m}\mu^{(i)}(k)\left(A^{(i)}x(k)+B^{(i)}u(k)+K^{(i)}e(k)\right) \\ y(k)=Cx(k)+Du(k)+e(k) \end{cases} \tag{8}$$

where $K$ is the Kalman filter gain, which has a time-varying functional relationship with the scheduling matrix $\mu(k)$, given by $K(\mu(k))=\sum_{i=1}^{m}\mu^{(i)}(k)K^{(i)}$. The innovation $e(k)$ represents zero-mean white noise.

Further define $\tilde{A}^{(i)}=A^{(i)}-K^{(i)}C$, $\tilde{B}^{(i)}=A^{(i)}-K^{(i)}D$, and rewrite (8) in predictor form

$$\begin{cases} x(k+1)=\sum_{i=1}^{m}\mu^{(i)}(k)\left(\tilde{A}^{(i)}x(k)+\tilde{B}^{(i)}u(k)+K^{(i)}y(k)\right) \\ y(k)=Cx(k)+Du(k)+e(k) \end{cases} \tag{9}$$

with

$$\tilde{A}(\mu(k))=\sum_{i=1}^{m}\mu^{(i)}(k)\tilde{A}^{(i)} \quad \tilde{B}(\mu(k))=\sum_{i=1}^{m}\mu^{(i)}(k)\tilde{B}^{(i)} \tag{10}$$

where the notation $\tilde{\bullet}$ denotes the predictive form, and the other matrices are similar to this one. Also, to simplify the subsequent symbolic representation, denote the system matrix of the scheduling matrix function by the separate $A_\mu(k)$, $B_\mu(k)$ and $K_\mu(k)$, i.e., $A_\mu(k)=A(\mu(k))$, $B_\mu(k)=B(\mu(k))$, $K_\mu(k)=K(\mu(k))$, $\tilde{A}_\mu(k)=\tilde{A}(\mu(k))$, $\tilde{B}_\mu(k)=\tilde{B}(\mu(k))$.

Under a reasonable assumption of system stability, we have $\tilde{A}_\mu(k+p-1)\approx 0$ for sufficiently larger user-defined parameters $p$. Thus by iterating (9) and neglecting the term about $\tilde{A}_\mu(k+p-1)$, then have

$$x(k+p)=\kappa_p N_p(k) Z_p(k) \tag{11}$$

where $\kappa_p$ is the extended controllability matrix, $N_p(k)$ denotes a known matrix containing only the scheduling matrix, $Z_p(k)$ is a matrix containing input and output information.

They are represented as follows:

$$\kappa_p=[L_p,\quad L_{p-1},\ldots,L_1] \tag{12}$$

$$L_1=[\bar{B}^{(1)},\ldots,\bar{B}^{(m)}] \tag{13}$$

$$L_j=[\tilde{A}^{(1)}L_{j-1},\ldots,\tilde{A}^{(m)}L_{j-1}] \tag{14}$$

with $\kappa_p\in\mathbb{R}^{n\times\tilde{q}}$, $\tilde{q}=(r+l)\cdot\sum_{j=1}^{p}m^j$, $\bar{B}^{(i)}=[\tilde{B}^{(i)},\quad K^{(i)}]$.

The matrix $N_p(k)$ contains the scheduling sequence presented as follows:

$$N_p(k)=\begin{bmatrix} R_p(k) & 0 & 0 & 0 \\ 0 & R_{p-1}(k+1) & 0 & 0 \\ \vdots & \vdots & \ddots & \vdots \\ 0 & 0 & 0 & R_1(k+p-1) \end{bmatrix} \tag{15}$$

$$R_p(k)=\mu(k+p-1)\otimes\cdots\otimes\mu(k)\otimes I_{r+l} \tag{16}$$

with $R_p(k)\in\mathbb{R}^{m^p(r+l)\times(r+l)}$ and $\otimes$ represents the Kronecker product.

The matrix $Z_p(k)$ contains the input–output data as follows:

$$Z_p(k)=[z(k)^\top,\quad z(k+1)^\top,\quad \ldots,z(k+p-1)^\top]^\top \tag{17}$$

$$z(k)=[u(k)^\top \quad y(k)^\top]^\top. \tag{18}$$

Substituting (11) into (9), can reconstruct the input–output behavior of the system without the influence of the state as follows:

$$y(k)=C\kappa_p\bar{Z}_p(k)+Du(k)+e(k) \tag{19}$$

where $\bar{Z}_p(k)=N_p(k-p)Z_p(k-p)$, the (19) indicates that the relationships between the internal and external variables of lithium-ion batteries can be reconstructed using a linear model. Thus, $C\kappa_p$ can be estimated within a linear computational framework.

### B. Estimation of $C\kappa_p$ With an Adaptive Strategy

Considering the time-varying nature of the model parameters and the need to dynamically adjust the model to track unknown parameters quickly, propose the adaptive forgetting factor recursive least squares (AFFRLS) method to solve the following objective function:

$$\arg_{\text{AFFRLS}}\min_{C\kappa_p,\,D}\sum_{k=1}^{N}\lambda_1^{N-k}\left\|y(k)-[C\kappa_p\quad D]\begin{bmatrix}\bar{Z}_p(k)\\ u(k)\end{bmatrix}\right\|^2 \tag{20}$$

where $N$ is the data length, $(\hat{.})$ denotes the estimate of $(.)$, and the forgetting factor $\lambda_1$ is a positive scalar between 0 and 1, controlling the influence of past data on the model.

Define $\hat{\theta}_1(k)=[\hat{C}(k)\hat{\kappa}_p(k)\quad \hat{D}(k)]$, and $\varphi_1(k)=[\bar{Z}_p(k)^\top \quad u(k)^\top]^\top$, the unknown parameters can be estimated using AFFRLS in an online form

$$\begin{cases} P_1(k) = \frac{1}{\lambda_1(k)} \cdot \frac{P_1(k-1)}{\lambda_1(k)+\varphi_1(k)^\top P_1(k-1)\varphi_1(k)} \\ \quad -\frac{P_1(k-1)[\varphi_1(k)\varphi_1(k)^\top]P_1(k-1)}{\lambda_1(k)+\varphi_1(k)^\top P_1(k-1)\varphi_1(k)} \\ \hat{e}_1(k) = y(k) - \hat{\theta}_1(k-1) \cdot \varphi_1(k) \\ \hat{\theta}_1(k) = \hat{\theta}_1(k-1) + e_1(k) \cdot \varphi_1(k)^\top \cdot P_1(k) \\ \lambda_1(k) = \lambda_{1\min} + (1-\lambda_{1\min}) \cdot h_1^{\varepsilon_1(k)} \\ \varepsilon_1(k) = \text{round}\left(\left(\frac{\hat{e}_1(k)}{e_{\text{base}}}\right)^2\right) \end{cases} \tag{21}$$

where $P_1(k)$ is the covariance matrix and $\hat{e}_1(k)$ is the error between the estimated and true values.

An *adaptive strategy* is introduced in (21), where $\lambda_1(k)$ is the forgetting factor that varies with the error of the recognition parameter, $\lambda_{1\min}$ is its minimum value, selected as 0.98 in this article. $h$ is the sensitivity coefficient, indicating how the forgetting factor responds to error, with a range of 0 to 1. A smaller $h$ results in a faster rate of change for the forgetting factor; thus, $h$ is set to 0.9 in this article. $e_{\text{base}}$ is the reference error value allowed in recognition, and round$(n)$ denotes the function that rounds $n$ to the nearest integer. Specifically, when the model parameter's value is very large, the corresponding prediction error also tends to be larger, thus a smaller value of the forgetting factor is assigned to ensure that the online identification has a faster convergence speed and reduces the identification error. Conversely, when the parameter change rate is relatively stable or small, a larger forgetting factor is needed to ensure the stability of the algorithm. The proposed adaptive strategy can achieve good stability and tracking capabilities for model identification.

### *C. Estimation of State*

In this section, estimate $x(k)$ based on the estimated results of $\hat{C}(k)\hat{\kappa}_p(k)$. To achieve this goal, the following lemmas about rank conditions are given first.

*Lemma 1:* For any matrices $A \in \mathbb{R}^{r_1 \times r_2}$ and $B \in \mathbb{R}^{r_2 \times r_3}$, the rank of $AB$ satisfies the following conditions:

$$\begin{aligned} \text{rank}(A) + \text{rank}(B) - r_2 &\le \text{rank}(AB) \\ &\le \min\{\text{rank}(A), \text{rank}(B)\}. \end{aligned} \tag{22}$$

*Lemma 2:* Assuming that the system (8) is controllable and observable, then the rank of observability matrice $\Gamma$ and controllability matrice $\kappa_p$ are equal to $n_x$, that is

$$\text{rank}(\Gamma) = \text{rank}\left(\left[C^\top, (C\Phi_1(k))^\top, \ldots, (C\Phi_p(k))^\top\right]^\top\right) \tag{23}$$

where the transfer matrix $\Phi_p(k)$ is $\Phi_p(k) = \tilde{A}_\mu(k+p-1)\tilde{A}_\mu(k+p-2)\cdots\tilde{A}_\mu(k)$.

Using the above lemmas, the rank of the product of the extended observability matrix $\Gamma$ and the extended controllability matrix $\kappa_p$ is $n_x$ shown as follows (24) shown at the bottom of this page: Furthermore, it follows from (11) that:

$$\Gamma\kappa_p\bar{Z}_p(k) = \Gamma x(k). \tag{25}$$

Because the rank of $\Gamma$, $x(k)$, and $\Gamma\kappa_p$ are $n_x$, and the matrix $Z_p(k)$ is of full rank, applying Lemma 1 once again, we have

$$\text{rank}(\Gamma\kappa_p\bar{Z}_p(k)) = \text{rank}(\Gamma x(k)) = n_x. \tag{26}$$

Which indicates that $x(k)$ can be estimated from $\Gamma\kappa_p\bar{Z}_p(k)$ using a low-rank extraction algorithm, which lies within the subspace spanned by the right $n_x$ columns of $\Gamma\kappa_p\bar{Z}_p(k)$. Considering the large dimensionality of matrix $\Gamma\kappa_p\bar{Z}_p(k)$, general low-rank approximation algorithms are not suitable for online updates. To facilitate online updates, employs the propagator method [31], [32]. To achieve this goal, a permutation method is proposed to estimate $x(k)$ from $\Gamma\kappa_p\bar{Z}_p(k)$.

Thus, the matrix $\Gamma\kappa_p$ can be re-expressed as follows form by constructing a permutation matrix $S \in \mathbb{R}^{(p-1)l \times (p-1)l}$ that may be chosen as an identity matrix:

$$S\Gamma\kappa_p = \begin{bmatrix} \Gamma\kappa_{p1} \\ \Gamma\kappa_{p2} \end{bmatrix} \tag{27}$$

where $\Gamma\kappa_{p1}$ is a block of $n_x$ linearly independent rows, i.e., $\text{rank}(\Gamma\kappa_{p1}) = n_x$, and $\Gamma\kappa_{p2} = P\Gamma\kappa_{p1}$ is a linear combination of $\Gamma\kappa_{p1}$.

Substituting (27) into (25), we have

$$\begin{aligned} S\Gamma\hat{x}(k) &= \begin{bmatrix} \Gamma\kappa_{p1} \\ \Gamma\kappa_{p2} \end{bmatrix} x(k) = \begin{bmatrix} I^n \\ P^\top \end{bmatrix} \Gamma\kappa_{p1}x(k) \\ &= \begin{bmatrix} I^n \\ P \end{bmatrix} \Gamma\kappa_{p1}\bar{Z}_p(k). \end{aligned} \tag{28}$$

This implies that the state can be estimated based on the following calculation:

$$\hat{x}(k) = \Gamma\hat{\kappa}_{p1}(k)\bar{Z}_p(k) \tag{29}$$

which means that $\hat{x}(k)$ can be easily chosen as the first $n_x$ elements of $\Gamma\kappa_p\bar{Z}_p(k)$ with $S = I$.

$$\Gamma\kappa_p = \begin{bmatrix} CL_p & CL_{p-1} & \ldots & CL_1 \\ C\tilde{A}\mu(k)L_p & C\tilde{A}\mu(k)L_{p-1} & \ldots & C\tilde{A}\mu(k)L_1 \\ C(\tilde{A})^2\mu(k+1)\mu(k)L_p & C(\tilde{A})^2\mu(k+1)\mu(k)L_{p-1} & \ldots & C(\tilde{A})^2\mu(k+1)\mu(k)L_1 \\ \vdots & \vdots & \ddots & \vdots \\ C(\tilde{A})^{p-1}\mu(k+p-2)\cdots\mu(k)L_p & C(\tilde{A})^{p-1}\mu(k+p-2)\cdots\mu(k)L_{p-1} & \ldots & C(\tilde{A})^{p-1}\mu(k+p-2)\cdots\mu(k)L_1 \end{bmatrix} \tag{24}$$

### *D. Estimation of the System Matrices*

Substituting the estimated states into system (8), obtain two regression equations. All system matrices can then be estimated using the AFFRLS method, similar to (21), as follows.

Define $\hat{\theta}_2(k) = [\hat{C}(k) \quad \hat{D}(k)]$, and $\varphi_2(k) = [\hat{x}(k)^\top \quad u(k)^\top]^\top$, and solve following regression problem,

$$\arg_{\text{AFFRLS}} \min_{C,\, D} \sum_{k=1}^{N} \lambda_2^{N-k} \left\| \hat{y}(k) - \hat{\theta}_2(k)\varphi_2(k) \right\|^2 \tag{30}$$

the unknown system matrices $C$ and $D$ can be estimated similarly to (21), more details as Algorithm 1.

Then, the innovation $\hat{e}(k)$ can be obtained shown as

$$\hat{e}(k) = y(k) - \hat{\theta}_2(k) \cdot \varphi_2(k). \tag{31}$$

Define $\hat{\theta}_3(k) = [\hat{A}(k) \quad \hat{B}(k) \quad \hat{K}(k)]$, and $\varphi_3(k) = [(\mu(k) \otimes \hat{x}(k))^\top \quad (\mu(k) \otimes u(k))^\top \quad (\mu(k) \otimes \hat{e}(k))^\top]^\top$, by solving following linear regression problem

$$\arg_{\text{AFFRLS}} \min_{A,\, B,\, K} \sum_{k=1}^{N} \lambda_3^{N-k} \left\| \hat{x}(k+1) - \hat{\theta}_3(k)\varphi_3(k) \right\|^2 \tag{32}$$

the unknown system matrices $A$, $B$, and $K$ can be estimated similarly to (21), more details as Algorithm 1.

It is straightforward from (30) and (32) to obtain

$$\hat{A}(k) = \hat{\theta}_3(k)(:, 1 : n_x \cdot m) \tag{33}$$

$$\hat{B}(k) = \hat{\theta}_3(k)(:, n_x \cdot m + 1 : n_x \cdot m + r \cdot m) \tag{34}$$

$$\hat{C}(k) = \hat{\theta}_2(k)(:, 1 : n_x) \tag{35}$$

$$\hat{D}(k) = \hat{\theta}_2(k)(:, n_x + 1 : n_x + r). \tag{36}$$

The matrices $\hat{A}^{(i)}(k)$, and $\hat{B}^{(i)}(k)$ can be directly extracted from $\hat{A}(k)$, and $\hat{B}(k)$, respectively.

For clarity, the proposed Adaptive Recursive Predictor-Based Subspace IDentification algorithm, based on the LTPV model in predictor form (abbreviated as LTPV+ARPBSID), is summarized in Algorithm 1. The corresponding algorithm flowchart is provided in Fig. 2 for easy reading.

## IV. SIMULATION STUDY

This section uses a MATLAB example to evaluate and compare the proposed method with several classical first-order ECM-based methods.

### *A. Reference Methods for Comparison*

To evaluate the performance of the proposed method, following three online estimation techniques based on first-order ECM are selected for comparison.

1) *The RLS method* [33]: RLS algorithm with forgetting factor $\lambda_{\text{RLS}} = 0.95$. 2) *The joint EKF method* [24] performs simultaneous estimation of model parameters using an observer that can be directly tuned for single-parameter adjustment. The observer uses a tuning parameter $\lambda_{\text{joint EKF}} = 0.9999$.

3) *The joint UKF method* [34] achieves simultaneous estimation of model parameters using the UKF technique.

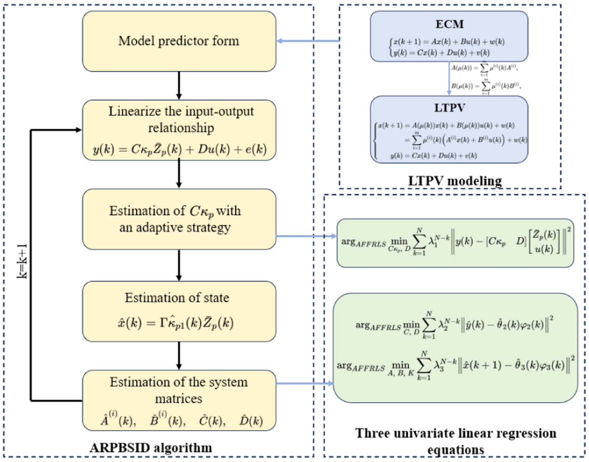

Fig. 2. LTPV+ARPBSID method flowchart.

### *B. Validation Metrics*

The quality of the proposed algorithm is evaluated using the mean absolute error (MAE) and the root mean square error (RMSE). MAE provides a clear measure of prediction error, while RMSE is highly sensitive to large or small errors, offering a precise reflection of measurement accuracy. The definitions of MAE and RMSE are as follows:

$$\text{MAE} = \frac{1}{N} \sum_{k=1}^{N} |\hat{y}(k) - y(k)| \tag{37}$$

$$\text{RMSE} = \sqrt{\frac{1}{N} \sum\nolimits_{k=1}^{N} (\hat{y}(k) - y(k))^2} \tag{38}$$

where $\hat{y}(k)$ is the output voltage estimated by the battery model at $k$th sampling point.

### *C. Simulation Result*

Consider a first-order ECM for $C_d = 1000$ F, $R_d = R_0 = 0.05\ \Omega$, SOC $= 80\%$, SOC–OCV curve fitted by the simulation model is $V_{\text{oc}} = 10.0364x^6 - 25.9659x^5 + 19.9378x^4 + 0.0161x^3 - 5.4184x^2 + 2.2809x + 3.2973$. To simulate the effects of changes in the aging and operating environment on the parameters, defined the model parameters as nonlinear changes over time as shown in Table I.

Note that the formulas in Table I are designed to simulate the cyclic aging of a battery during charging or discharging. In the study of the cycle test using the mixed pulse current distribution as excitation [33], [35], [36], $R_0$, $R_d$ and the test time exhibit a nonlinear increase, while the values of $C_d$ and $C_n$ exhibit a nonlinear decrease. To simulate this aging effect, assume that the model parameters $R_0$ and $C_d$ are a function that changes slowly over time within a period, and (39)–(42) represent the trend of change for these model parameters. In [37] indicates that the model response is almost insensitive to perturbations in parameters $R_d$ and $C_d$, and $R_0$ is the dominant parameter of the change in response, so pay more attention to the change in $R_0$ in the simulation study. According to [38], changes in the operating environment, especially temperature, will cause

**Algorithm 1:** LTPV+ARPBSID Algorithm.

```
Input: $u(k)$, $y(k)$, $\mu(k)$
Initialization: $p$, $f$, $n$, $P_{1,2,3}$, $\lambda_{1,2,3}$
for $k = p+1, p+2, \ldots$ do
    Reconstruct $y(k)$ using (19)
    Compute $\hat{C}(k)\hat{\kappa_p}(k)$ using (20)
    $\begin{cases} P_1(k) = \frac{1}{\lambda_1(k)} \cdot \frac{P_1(k-1)}{\lambda_1(k) + \varphi_1(k)^\top P_1(k-1)\varphi_1(k)} \\ \quad - \frac{P_1(k-1)[\varphi_1(k)\varphi_1(k)^\top]P_1(k-1)}{\lambda_1(k) + \varphi_1(k)^\top P_1(k-1)\varphi_1(k)} \\ \hat{e}_1(k) = y(k) - \hat{\theta}_1(k-1) \cdot \varphi_1(k) \\ \hat{\theta}_1(k) = \hat{\theta}_1(k-1) + e_1(k) \cdot \varphi_1(k)^\top \cdot P_1(k) \\ \lambda_1(k) = \lambda_{1min} + (1 - \lambda_{1min}) \cdot h_1^{\varepsilon_1(k)} \\ \varepsilon_1(k) = round\left(\left(\frac{\hat{e}_1(k)}{e_{base}}\right)^2\right) \end{cases}$
    Estimate state $\hat{x}(k)$ using (29)
    Estimate system matrices using (31) and (32)
    $\begin{cases} P_2(k) = \frac{1}{\lambda_2(k)} \cdot \frac{P_2(k-1)}{\lambda_2(k) + \varphi_2(k)^\top P_2(k-1)\varphi_2(k)} \\ \quad - \frac{P_2(k-1)[\varphi_2(k) \cdot \varphi_2(k)^\top]P_2(k-1)}{\lambda_2(k) + \varphi_2(k)^\top P_2(k-1)\varphi_2(k)} \\ \hat{e}_2(k) = y(k) - \hat{\theta}_2(k-1) \cdot \varphi_2(k) \\ \hat{\theta}_2(k) = \hat{\theta}_2(k-1) + e_2(k) \cdot \varphi_2(k)^\top \cdot P_2(k) \\ \lambda_2(k) = \lambda_{2min} + (1 - \lambda_{2min}) \cdot h_2^{\varepsilon_2(k)} \\ \varepsilon_2(k) = round\left(\left(\frac{\hat{e}_2(k)}{e_{base}}\right)^2\right) \end{cases}$
    $\hat{e}(k) = y(k) - \hat{\theta}_2(k) \cdot \varphi_2(k).$
    $\begin{cases} P_3(k) = \frac{1}{\lambda_3(k)} \cdot \frac{P_3(k-1)}{\lambda_3(k) + \varphi_3(k)^\top P_3(k-1)\varphi_3(k)} \\ \quad - \frac{P_3(k-1)[\varphi_3(k)\varphi_3(k)^\top]P_3(k-1)}{\lambda_3(k) + \varphi_3(k)^\top P_3(k-1)\varphi_3(k)} \\ \hat{e}_3(k) = \hat{x}(k) - \hat{\theta}_3(k-1) \cdot \varphi_3(k) \\ \hat{\theta}_3(k) = \hat{\theta}_3(k-1) + e_3(k) \cdot \varphi_3(k)^\top \cdot P_3(k) \\ \lambda_3(k) = \lambda_{3min} + (1 - \lambda_{3min}) \cdot h_3^{\varepsilon_3(k)} \\ \varepsilon_3(k) = \text{round}\left(\left(\frac{\hat{e}_3(k)}{e_{base}}\right)^2\right) \end{cases}$
Compute $\hat{A}^{(i)}(k)$, $\hat{B}^{(i)}(k)$, $\hat{C}(k)$, and $\hat{D}(k)$ using (33)-(36)
```

significant changes in $R_0$. Therefore, assume that $R_0$ changes during the time intervals $t = 2000$–$3000$ s and $t = 7000$–$8000$ s of each cycle due to changes in the operating environment. Equation (43) describes the relation that causes a sharp change in $R_0$.

To comprehensively validate the superiority of the proposed method, this section systematically designs seven sets of comparative simulations (Test 1–Test 8) in the following parts.

*1) Test 1 (Comparison of Linear Methods):* This article employs the LTPV + ARPBSID method with a model order $n_x$=2, a covariance matrix $P_1 = 100$, and other covariance matrices $P_{2,3}$ set to $10^{-5}$. The minimum values for $\lambda_{1\min}$, $\lambda_{2\min}$, and $\lambda_{3\min}$ are set to 0.98, user-defined parameters $p = 5$, and system matrices as well as other matrices are initialized to minimal values (e.g., $10^{-8}$). The scheduling matrix $\mu(k)$ comprises two variables: $\mu^{(1)}(k)$, which represents SOC due to its close relationship with lithium battery performance and its ease of measurement [39], and $\mu^{(2)}(k) = \text{SOC}^2(k) + \text{SOC}(k)$. The inclusion of the higher-order term introduces a nonlinear relationship between variables, while the polynomial form ensures smoother system operation. The polynomial coefficients can be adjusted based on control accuracy to maintain system stability.

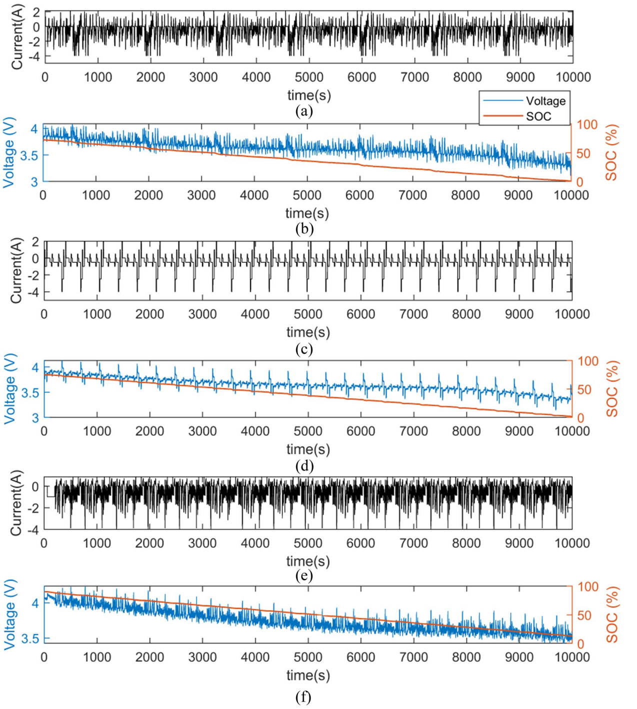

Fig. 3. Typical working condition current excitation, voltage and SOC. (a) FUDS current excitation. (b) FUDS voltage and SOC. (c) DST current excitation. (d) DST voltage and SOC. (e) UDDS current excitation. (f) UDDS voltage and SOC.

Three typical working conditions current excitation [Federal Urban Driving Schedule (FUDS), Dynamic Stress Test (DST), and Urban Dynamometer Driving Schedule (UDDS)] are were, respectively, fed to the model as shown in Fig. 3(a)–(e). The resulting terminal voltages were sampled with a sampling period of $T_s = 1$ s, and the SOC was calculated using the coulomb counting equation $\text{SOC}(k) = \text{SOC}(0) - \frac{\int i\,dt}{C_n}$, as shown in Fig. 3(b)–(f). This section simulates the changes in battery characteristics caused by long-term aging of the battery. Therefore, the battery parameters are set for cyclic aging, the parameter settings for 20 cycles are shown in Fig. 4, and details can be found in Test 3. To simulate real-life noise interference, white noise with variances of $\delta_i^2 = 1\,(\text{mA}^2)$ and $\delta_v^2 = 1\,(\text{mV}^2)$ was added to the signals.

The comparison results of current excitation under three typical working conditions in the linear method are shown in Fig. 5, which indicates that all four methods can accurately track the true output voltage with optimal errors controlled within 0.05 V. However, RLS, joint EKF and joint UKF perform worse than LTPV+ARPBSID. All three comparison methods are identification algorithms that rely on traditional ECMs. Traditional ECMs simulate battery behavior exclusively through

TABLE I
PARAMETER CHANGES

| Parameter | Aging function | Initial value | Label |
|---|---|---|---|
| $R_d$ | $R_d(k+1) = R_d(k) + 0.01 \times \frac{e^{-\frac{k+7000}{2000}}-1}{e^{-1}-1} - 0.01534$ | $R_d(0) = 0.05\,\Omega$ | (39) |
| $C_d$ | $C_d(k+1) = C_d(k) - \frac{e^{-\frac{k+1000}{2000}}-1}{e^{-1}-1} + 0.6$ | $C_d(0) = 1000\,\mathrm{F}$ | (40) |
| $C_n$ | $C_n(k+1) = C_n(k) + 936 \times \frac{e^{-\frac{k+6000}{2000}}-1}{e^{-1}-1} + 0.0195$ | $C_n(0) = 7200\,\mathrm{As}$ | (41) |
| $R_0^{aging}$ | $R_0^{aging}(k+1) = R_0^{aging}(k) + \frac{e^{-\frac{k+7000}{2000}}-1}{50\times(e^{-1}-1)} - 0.03068$ | $R_0(0) = 0.05\,\Omega$ | (42) |
| $R_0$ | $R_0(k+1) = \begin{cases} R_0(k) + \frac{e^{-\frac{k+7000}{2000}}-1}{50\times(e^{-1}-1)} - 0.03068, & 1 \le k < 2000 \\ R_0(k) + \frac{e^{-\frac{k+7000}{2000}}-1}{50\times(e^{-1}-1)} - 0.030678, & 2000 \le k < 3000 \\ R_0(k) + \frac{e^{-\frac{k+7000}{2000}}-1}{50\times(e^{-1}-1)} - 0.03068, & 3000 \le k < 7000 \\ R_0(k) + \frac{e^{-\frac{k+7000}{2000}}-1}{50\times(e^{-1}-1)} - 0.030678, & 7000 \le k < 8000 \\ R_0(k) + \frac{e^{-\frac{k+7000}{2000}}-1}{50\times(e^{-1}-1)} - 0.03068, & k \ge 8000 \end{cases}$ | $R_0(0) = 0.05\,\Omega$ | (43) |

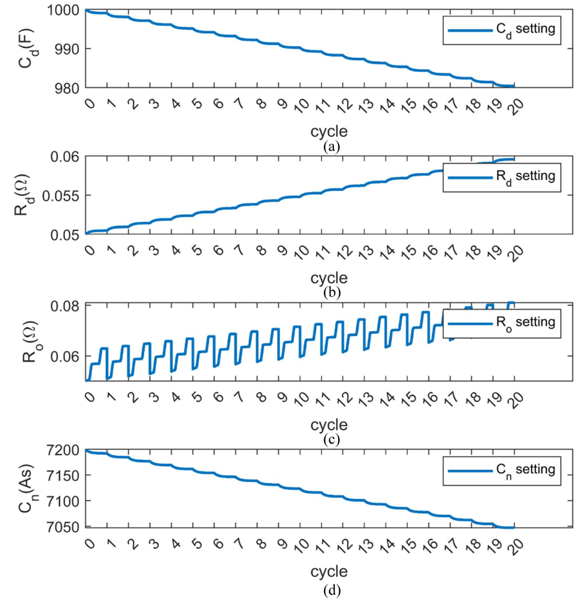

Fig. 4. Long-term aging parameter settings (20 cycles as an example). (a) $C_d$ cycle change settings. (b) $R_d$ cycle change settings. (c) $R_0$ cycle change Settings. (d) $C_n$ cycle change settings.

electrical components. As such, they are unable to fully capture the internal reactions and external characteristics of the battery. These models often neglect various internal and external factors, resulting in insufficient accuracy. They frequently fail to achieve satisfactory performance in subsequent model-based identification tasks. The results show that the LTPV+ARPBSID method proposed in this article, along with the three ECM-based online identification algorithms, can accurately track the real terminal voltage of the battery under time-varying parameters and aging conditions. Among them, LTPV+ARPBSID exhibits superior tracking performance compared to the other three methods.

To further quantify the accuracy of the four methods, the corresponding results of MAE and RMSE in Table II. The

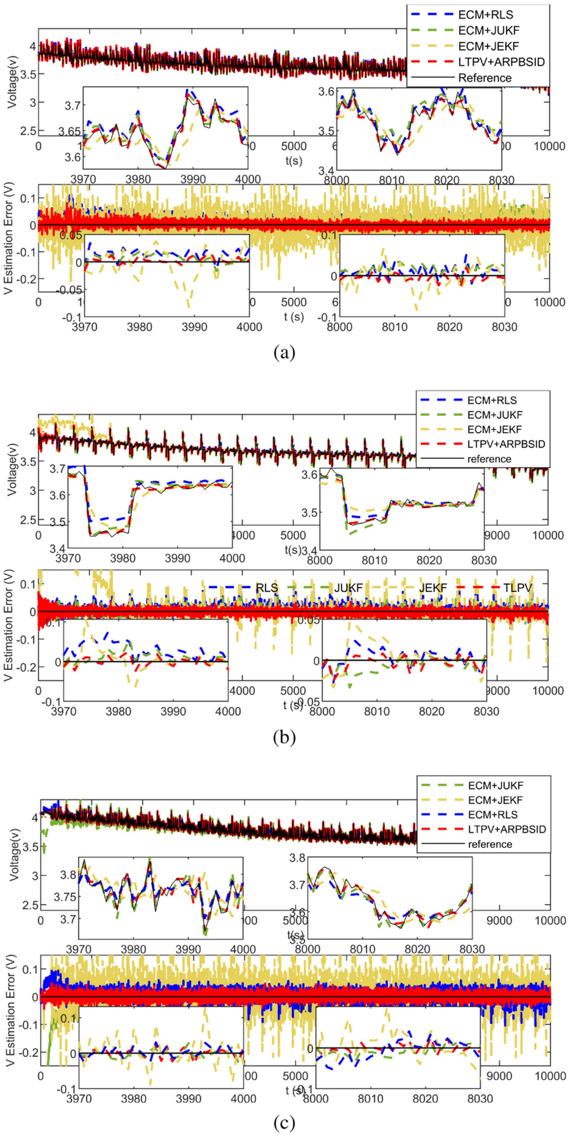

Fig. 5. The comparison results of linear methods. (a) Using FUDS current excitation. (b) Using DST current excitation. (c) Using UDDS current excitation.

TABLE II
STATISTICS FOR TYPICAL WORKING CONDITION SIMULATIONS

| | | ECM+RLS | ECM+Joint UKF | ECM+Joint EKF | LTPV+ARPBSID |
|---|---|---|---|---|---|
| FUDS current excitation | MAE | 6.9mV | 10.2mV | 17.7mV | **3.4mV** |
| | RMSE | 12.4mV | 35.2mV | 58.2mV | **5.9mV** |
| DST current excitation | MAE | 24.9mV | 14.6mV | 48.1mV | **8.7mV** |
| | RMSE | 113.7mV | 42.7mV | 140.8mV | **11.9mV** |
| UDDS current excitation | MAE | 33.2mV | 30.9mV | 34.5mV | **11.1mV** |
| | RMSE | 113.1mV | 77.8mV | 51.9mV | **16.0mV** |

TABLE III
COMPUTATIONAL BURDEN PER RECURSION

| RLS | joint EKF | joint UKF | ARPBSID |
|---|---|---|---|
| $(n_x+2)^2$ | $(n_x+3)^2$ | $(n_x+3)^2$ | $p^2+(\tilde{q}+r)^2+(n_x+r)^2+s^2(n_x+r+l)^2$ |

optimal MAE of the LTPV+ARPBSID method is approximately 3.4 mV, which is better than that of the other three algorithms. This numerically verifies the effectiveness of the method.

*2) Test 2 (Comparison of Computational Burden):* On the other hand, in theoretical terms, the computational complexity of the four schemes is compared as shown in Table III. It can be seen that the calculation amount of the ARPBSID algorithm proposed in this article is slightly higher than that of the first three schemes due to the need to process a large number of nonlinear data to linearize it and the adaptive forgetting factor added to deal with the impact of battery aging and degradation. However, by observing the simulation results, as shown in Fig. 5, the scheme provides higher accuracy for the aging battery model without adding too much computational effort. Therefore, the ARPBSID algorithm still has great potential in the application of identifying aging battery models.

*3) Test 3 (Comparison of Different Aging Degrees):* To evaluate the model's capability under the influence of more internal and external factors, and to compare its accuracy and robustness under different aging conditions, this section introduces the comparison of batteries under different degrees of aging. The cycle aging behavior of $C_n$, $C_d$, $R_d$, and $R_0$ is simultaneously defined to more accurately characterize the battery's dynamic behavior during battery degradation. It is assumed that all cycles under the same cycling test have an equal impact on cycle aging and that the aging effect of each cycle is irreversible. After determining the initial parameter values for each cycle, the parameters are updated within each cycle based on Table I. The current input cycle test is then repeated, with the parameter values at the end of one cycle serving as the initial values for the next. The parameter variation functions between cycles are shown as follows:

$$C_d{}^{\text{cycle}(i)}(0) = C_d{}^{\text{cycle}(i-1)}(kT) \tag{44}$$

$$R_d{}^{\text{cycle}(i)}(0) = R_d{}^{\text{cycle}(i-1)}(kT) \tag{45}$$

$$R_0{}^{\text{cycle}(i)}(0) = R_{0_{\text{aging}}}^{\text{cycle}(i-1)}(kT) \tag{46}$$

$$C_n{}^{\text{cycle}(i)}(0) = C_n{}^{\text{cycle}(i-1)}(kT) \tag{47}$$

where the parameter $C_d{}^{\text{cycle}(i)}(0)$, $R_d{}^{\text{cycle}(i)}(0)$, $R_0{}^{\text{cycle}(i)}(0)$, and $C_n^{\text{cycle}(i)}(0)$ are the initial value of $C_d$, $R_d$, $R_0$, and $C_n$ at cycle $i$, respectively; $C_d{}^{\text{cycle}(i-1)}(kT)$, $R_d{}^{\text{cycle}(i-1)}(kT)$, and $C_n{}^{\text{cycle}(i-1)}(kT)$ are the last value of $C_d$, $R_d$, and $C_n$ at cycle $i$-1, respectively; $R_{0_{\text{aging}}}^{\text{cycle}(i-1)}(kT)$ is the last value of $R_0$ at cycle $i$-1 under aging only. $kT$ is the number of time steps in each cycle. Table I simulates the slow changes in battery characteristics within a single cycle due to interference factors such as current fluctuations and temperature variations, describing the detailed characteristics of parameter changes. Equations (44)–(47) simulate the trend of parameter variations between adjacent cycles, illustrating the general trend of parameter changes. Fig. 4 shows the long-term aging trend over 20 cycles.

The input current follows the FUDS profile [as shown in Fig. 3(a)], with voltage sampled at $T_s = 1$ s, and SOC calculated using the coulomb counting method. The initial values of $C_n$, $C_d$, $R_d$, and $R_0$ before cycling, as well as the initial parameters for all methods, are provided above. The resulting voltage and SOC after four sets of battery aging cycles (20 cycles, 100 cycles, 200 cycles, and 500 cycles) are shown in Fig 6. The results, as shown in Fig. 7, indicate that the proposed method maintains high accuracy and robustness under different aging and degradation conditions.

*4) Test 4 (Comparison of Noise Effects):* To assess the robustness of the proposed method under noise pollution, white noise is applied to the simulated battery's voltage and current signals over 20 cycles. The noise level is represented by the Signal-to-Noise Ratio (SNR), and the relationship between the SNR and the noise amplitude is given by

$$\text{SNR} = 10\log_{10}\left[\left(\frac{A_{\text{signal}}}{A_{\text{noise}}}\right)^2\right] = 20\log_{10}\left(\frac{A_{\text{signal}}}{A_{\text{noise}}}\right) \tag{48}$$

where $A_{\text{noise}}$ is amplitude of noise, and $A_{\text{signal}}$ is amplitude of real signal.

The output voltage identification results under added noise are shown in Figs. 8 and 9, where MAE and RMSE are used as measures of estimation accuracy. It can be observed that the cyclic degradation of parameters and the presence of noise introduce varying degrees of deviation in the identification results of

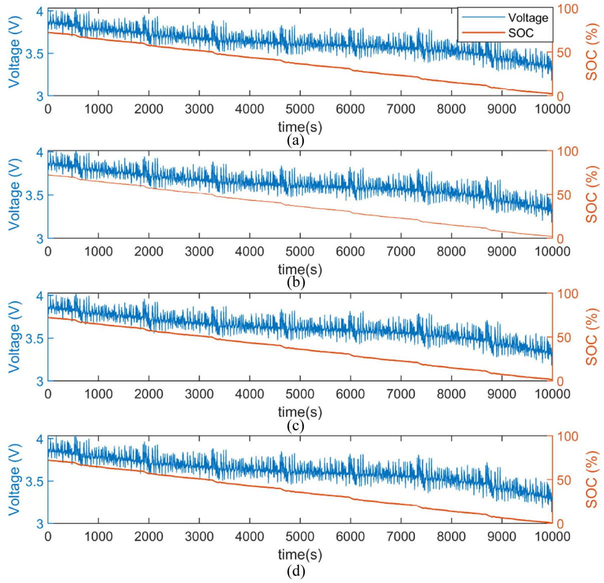

Fig. 6. Data details of different degrees of aging. (a) Voltage and SOC after 20 cycles. (b) Voltage and SOC after 100 cycles. (c) Voltage and SOC after 200 cycles. (d) Voltage and SOC after 500 cycles.

the four methods. However, under the same cycle and the same noise level, the proposed LTPV+ARPBSID method achieves better estimation results in both MAE and RMSE compared to the other three methods. From an overall perspective, when both the input and voltage measurements are affected by noise and parameter degradation, the changes in MAE and RMSE for LTPV+ARPBSID remain small, with less variation than those of the other three methods. This shows that LTPV+ARPBSID has better robustness to noise and is less affected by noise interference.

*5) Test 5 (Prefiltering Under Noise Corruption):* As demonstrated in Figs. 8 and 9, noise interference significantly compromises the accuracy of system identification, leading to inevitable model performance degradation if left unaddressed. Inspired by the preceding description, this section considers noise filtering for the input and output signals. Provide a signal corrupted by high-intensity noise, the voltage fitting results under strong noise interference [see Fig. 10(a)] reveal that while all four compared methods suffer from varying degrees of deviation caused by noise corruption, the proposed LTPV+ARPBSID method exhibits the smallest deviation magnitude and strongest noise resistance.

Since noise typically manifests as high-frequency signal components, the application of a low-pass filter can effectively achieve frequency-domain separation between noise and useful signals. Inspired by the preceding description, without modifying the methodological framework, a prefiltering can be integrated to enable the suppression or removal of noise. To validate the effectiveness of this approach, this chapter first presents a signal contaminated with high-intensity noise, the voltage fitting results under strong noise interference [see Fig. 10(a)] reveal that while all four compared methods suffer from varying degrees of deviation caused by noise corruption, the proposed LTPV+ARPBSID method exhibits the smallest deviation magnitude and strongest noise resistance.

Since noise typically manifests as high-frequency signal components, using a low-pass filter can effectively separate the noise from the useful signal in the frequency domain. Objectively, low-pass filtering of the useful signal can be achieved in many ways, such as adding resistors, capacitors, and other structures in the circuit to create an analog low-pass filter, or using digital filters like the Butterworth or Chebyshev filters based on transfer functions. This section considers using the built-in $lowpass$ function in MATLAB 2022a for low-pass filtering. The $lowpass$ function only needs to be preprocessed within the algorithm, without altering the original method framework, to suppress or remove noise. The specific setup of the low-pass filter is as follows: using the "$lowpass(signal, fpass, fs)$," where $signal$ is the input signal $u(k)$ and output signal $y(k)$ corrupted by noise. $fpass$ is the pass band frequency (i.e., the cutoff frequency), in BMSs, the cutoff frequency of the low-pass filter is generally set between 50–100 Hz. Therefore, set it to 60 Hz. And $fs$ is the sampling frequency, the sampling frequency in this section is 1 Hz. The configured low-pass filter is placed in front of the ARPBSID algorithm to preprocess the input signal corrupted by noise. After filtering, the identification steps can proceed as normal. The result of applying the filtering process, as shown in Fig. 10(b), all methods recover correct estimation values, but LTPV+ARPBSID maintains superior accuracy. These findings collectively demonstrate both the effective noise suppression capability of low-pass filtering for high-frequency interference and the sustained performance advantage of the proposed method in parameter identification under noise-attenuated conditions.

*6) Test 6 (Comparison of Nonlinear Methods):* The aforementioned simulations have verified that LTPV+ARPBSID demonstrates superior accuracy and robustness compared to online methods based on linear models. To comprehensively evaluate the method's performance, this section will conduct further comparative analysis between LTPV+ARPBSID and neural network approaches that possess nonlinear characterization capabilities. LTPV+ARPBSID and the three model-based methods use the same initial data and parameter settings as mentioned earlier. The neural network method is implemented using the MATLAB 2022a Neural Network Toolbox, with the training set consisting of the first 5000 data points from Fig. 3(a) and (b), and the test set including all 10 000 data points. Training is set to 70%, validation is set to 15%, Testing is set to 15%, and featuring a 10-neuron hidden layer. The Levenberg–Marquardt algorithm is used to train the neural network. After training, the neural network model achieves a coefficient of determination ($R^2$) of 99.88%.

The predicted results are shown in Fig. 11, MAE $=$11.4 mV and RMSE $=$14.7 mV. The voltage prediction curve based on the neural network toolbox (NF, purple dashed line) indicates that although the model performs well on the first 5000 training data points with a high goodness of fit ($R^2 = 99.88\%$), its performance significantly deteriorates when applied to predict the full dataset. This suggests that despite the large amount of training data providing a good initial fit, the neural network method struggles to offer online corrections for subsequent predictions,

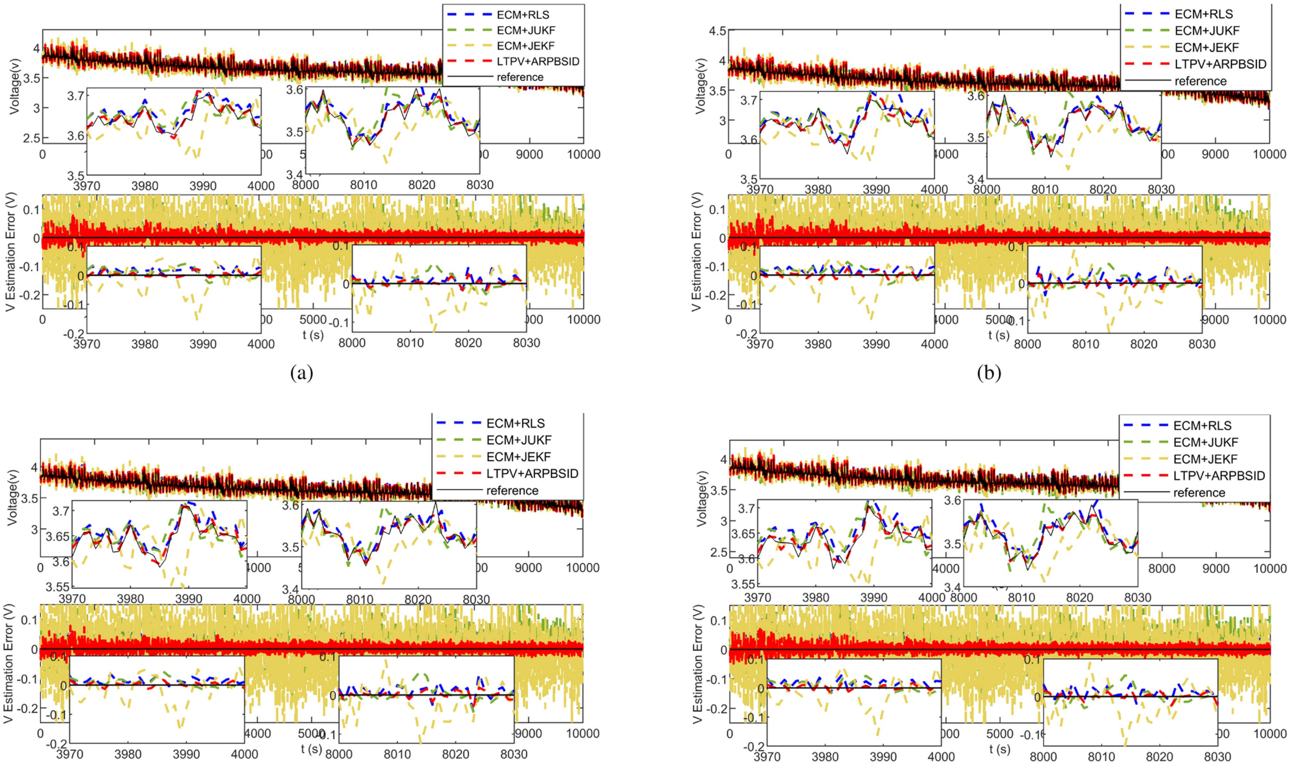

(a) (b)

(c) (d)

Fig. 7. The comparison result of battery degradation. (a) The voltage estimation result after 20 cycles. (b) The voltage estimation result after 100 cycles. (c) The voltage estimation result after 200 cycles. (d) The voltage estimation result after 500 cycles.

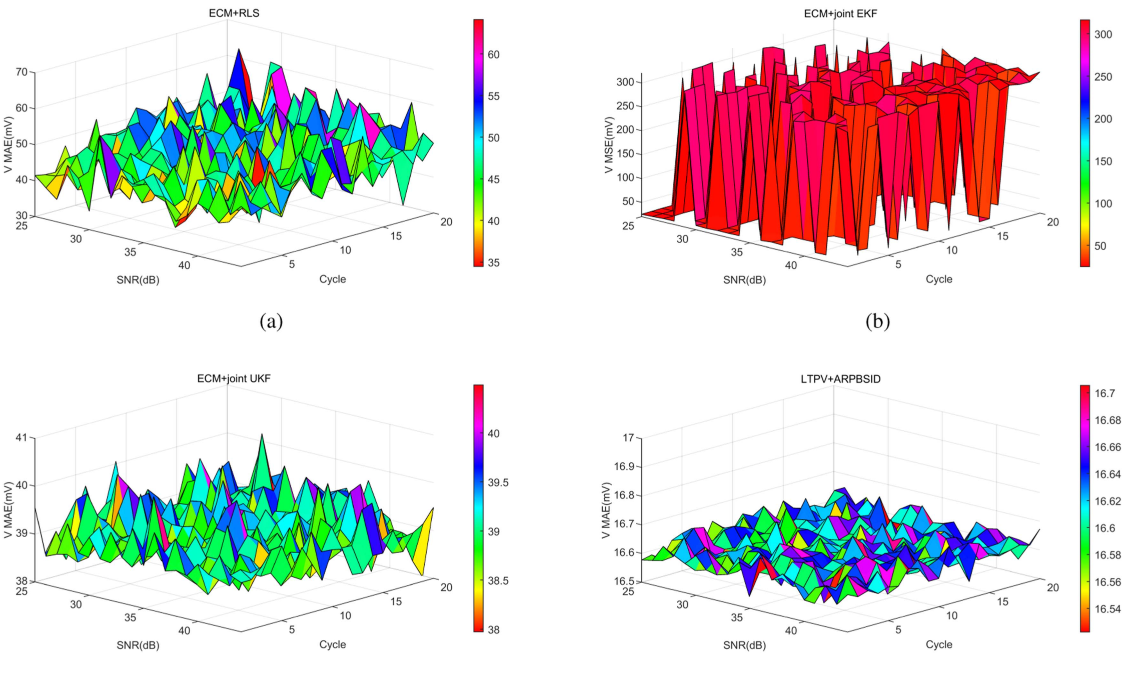

(a) (b)

(c) (d)

Fig. 8. MAE estimation results of output voltage under different SNR (dB) and cycle. (a) ECM+RLS. (b) ECM+joint EKF. (c) ECM+joint UKF. (d) LTPV+ARPBSID.

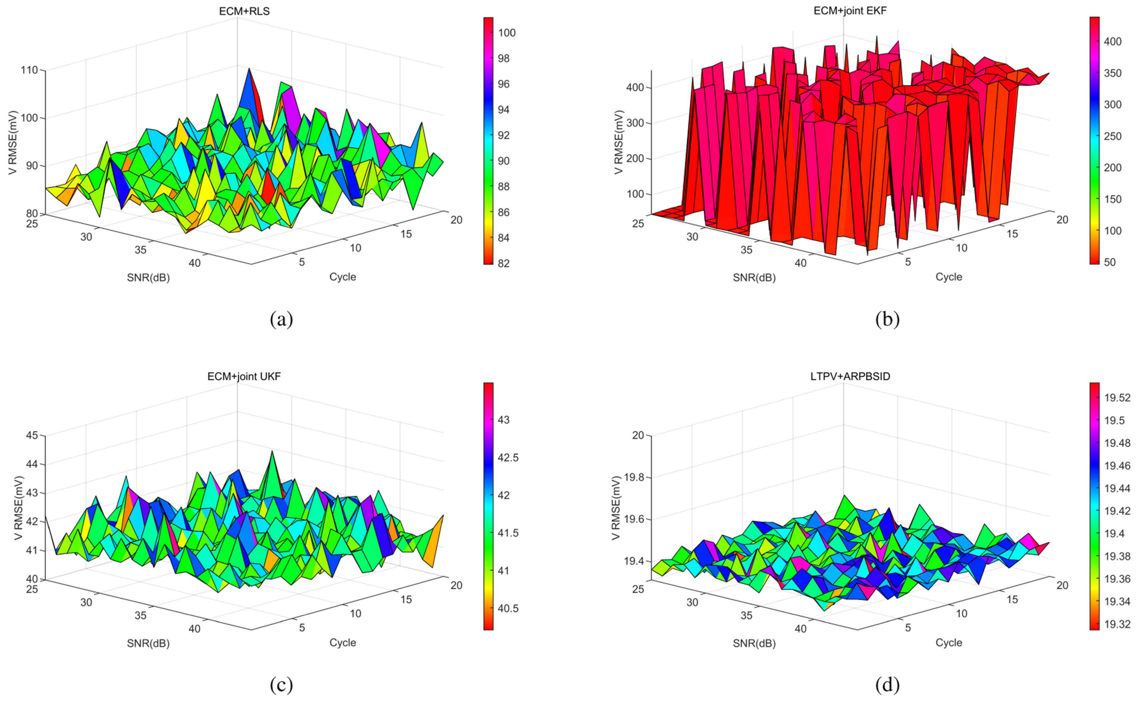

(a) (b) (c) (d)

Fig. 9. RMSE estimation results of output voltage under different SNR (dB) and cycle. (a) ECM+RLS. (b) ECM+joint EKF. (c) ECM+joint UKF. (d) LTPV+ARPBSID.

and it lacks the online adaptability to dynamic environmental changes. In contrast, the LTPV+ARPBSID method effectively overcomes this limitation through its adaptive strategy.

*7) Test 7 (Comparison of Applied to the ECM):* In the simulation analysis above, the scheduling matrix $\mu(k)$ of the LTPV model exhibits a nonlinear relationship with respect to SOC, demonstrating its effectiveness in improving the model's accuracy. This section will further apply the ARPBSID algorithm to a first-order ECM for a comprehensive analysis and compare the advantages of different algorithms. As shown in (8), when the scheduling matrix $\mu(k) = 1$, the LTPV model simplifies to a traditional ECM. To achieve this, an additional scheduling matrix $\mu(k) = 1$ is set, with the state variable $n_x = 2$, while the remaining initial parameters remain consistent with those in Test 1. The input–output data and SOC values are shown in Fig. 3(a) and (b).

The experimental results are shown in Fig. 12. The legend "LTPV+ARPBSID(1)" (light blue dashed line) represents the simulation results when the scheduling matrix is set to 1, indicating the application of the ARPBSID algorithm to the traditional first-order ECM. The "LTPV+ARPBSID" (red dashed line) represents the simulation results when the scheduling matrix takes a nonlinear form with respect to SOC. The results show that when the scheduling matrix is set to 1, the fitting performance of the ARPBSID algorithm is inferior to that of the nonlinear form fitting results shown by the red line, but it still outperforms other methods such as RLS in terms of fitting accuracy. In addition, when the ARPBSID algorithm is applied to the ECM, initial oscillations occur, and the time required to reach stability is longer compared to other methods.

*8) Test 8 (Comparison of Model Order):* In addition, the number of RC branches in the ECM is equivalent to $n_x$-1. As evident from (2), increasing the number of RC branches results in higher-dimensional system matrices, which consequently contain a greater number of nonzero elements. This, in turn, impacts system performance through the characteristics of the system matrices. Therefore, this chapter will further explore the specific influence of the system order on the proposed model.

The comparative experiments on system order will continue to utilize data generated from simulated circuits [see Fig. 3(a) and (b)], along with all initial variables. In these experiments, only $n_x$ is varied. As evident from the results presented in Fig. 13, higher-order LTPV models exhibit better voltage fitting and smaller errors; however, this effect diminishes over time. Notably, compared to the first-order model (depicted by the red line), higher-order models indeed provide increased precision during the initial identification phase, reduce the oscillation amplitude, and facilitate faster system stabilization. In addition, in actual program execution, higher-order models tend to run slower compared to when $n_x$=2. Therefore, the LTPV model, an extension of the ECM, follows a similar principle in terms of order selection. However, higher-order models increase structural complexity and computational difficulty (see Table III). The system order should be chosen based on practical circumstances to balance accuracy and computational complexity. To more intuitively compare the impact of system order on model performance, Table IV provides two statistical measures: MAE and RMSE.

In practical applications, one can choose an appropriate system order based on the computational power and precision

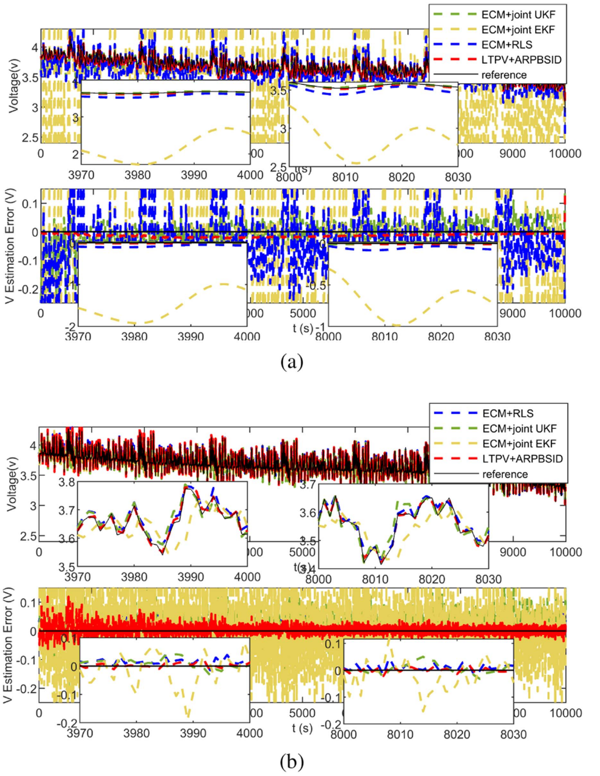

(a)

(b)

Fig. 10. Simulation study. (a) Voltage estimation results under noise damage. (b) Voltage estimation results after noise filtering.

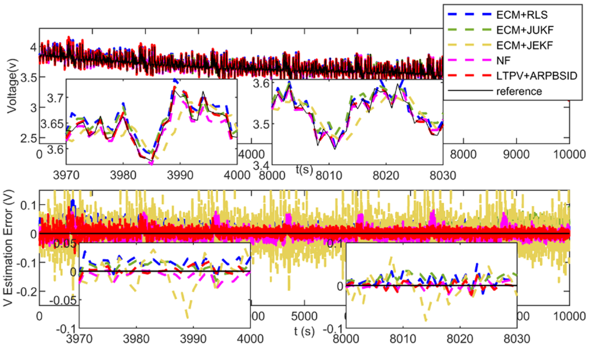

Fig. 11. Comparison results of linear and nonlinear methods.

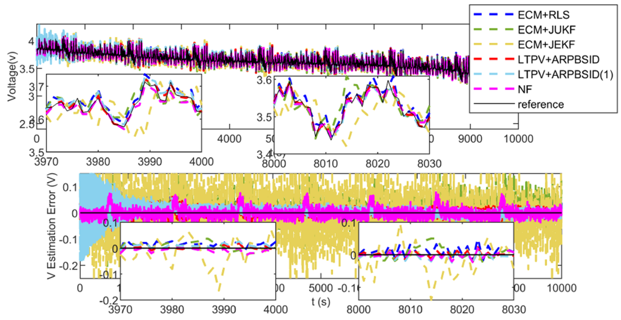

Fig. 12. Comparison results of the ARPBSID algorithm applied to ECM.

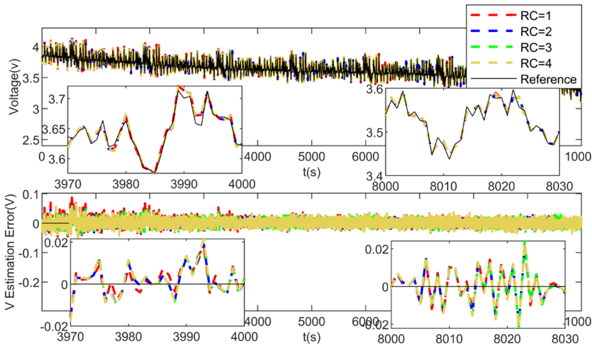

Fig. 13. Voltage estimation results of different orders.

TABLE IV
STATISTICS FOR SYSTEM ORDER COMPARISON

| RC branches | 1 | 2 | 3 | 4 |
|---|---|---|---|---|
| MAE | 3.1mV | 3.2mV | 3.4mV | 3.6mV |
| RMSE | 5.4mV | 5.6mV | 5.4mV | 6.0mV |

TABLE V
EXPERIMENTAL BATTERY PARAMETER INFORMATION

| Battery | Battery Parameter | Specifications Value |
|---|---|---|
| CS2 Battery | Nominal Capacity | 1.1 Ah |
| | Nominal Voltage | 4.2 V |
| | Operating Voltage Range | 2.7 V - 4.2 V |
| | Maximum Current | 1 C |
| $LiFePO_4$ Battery | Nominal Capacity | 94 Ah |
| | Nominal Voltage | 3.2 V |
| | Operating Voltage Range | 2.5 V - 3.65 V |
| | Max. Cont. Current | 2 C |
| 18650-NCM Battery | Nominal Capacity | 2 Ah |
| | Nominal Voltage | 3.6 V |
| | Operating Voltage Range | 2.5 V - 4.2 V |
| | Max. Cont. Current | 2 C |

requirements of the algorithm running on the device. For the subsequent verification of algorithm effectiveness in this article, will still adopt $n_x$=2.

## V. EXPERIMENTAL RESULT AND ANALYSIS

In this section, compare the performance of the proposed method against reference methods described in Section IV-A with two types aged batteries under real application conditions.

### A. The Experiment on CS2 Aged Battery

The experimental data set for the CS2 battery was provided by the battery research group at the Center for Advanced Life Cycle Engineering at the University of Maryland [40]. The battery is a lithium oxide cobalt battery containing trace manganese, the specific parameters are shown in Table V. The battery in the aging experiment all use the same charging curve, using the standard constant current/constant voltage protocol, the constant current rate is 0.5 C, after charging to 4.2 V, maintain 4.2 V until the current drops below 0.05 A. The battery is then fully

TABLE VI
STATISTICS FOR AGING BATTERY EXPERIMENTS

| | | ECM+RLS | ECM+Joint UKF | ECM+Joint EKF | LTPV+ARPBSID |
|---|---|---|---|---|---|
| CS2 Battery | MAE | 138.2mV | 120.9mV | 164.5mV | **51.8mV** |
| | RMSE | 227.8mV | 184.8mV | 460.0mV | **64.4mV** |
| $LiFePO_4$ Battery | MAE | 38.5mV | 20.8mV | 22.3mV | **13.6mV** |
| | RMSE | 46.1mV | 29.1mV | 30.7mV | **16.0mV** |
| 18650-NCM Battery | MAE | 53.0mV | 96.7mV | 105.2mV | **18.7mV** |
| | RMSE | 69.5mV | 109.9mV | 124.8mV | **21.3mV** |

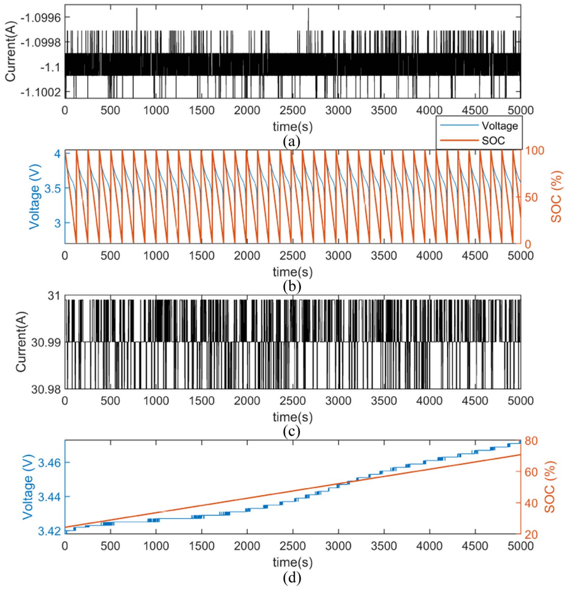

Fig. 14. Aged battery data details. (a) The input current in the CS2 battery. (b) The output voltage and SOC in the CS2 battery. (c) The input current in the $\text{LiFePO}_4$ battery. (d) The output voltage and SOC in the $\text{LiFePO}_4$ battery.

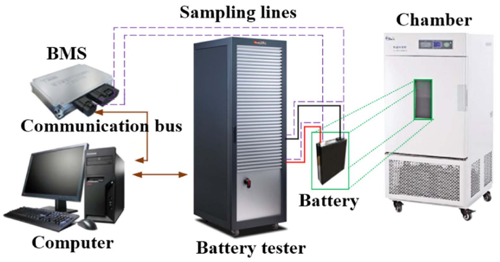

Fig. 15. Power battery test system.

discharged with a discharge current of 1 C until the discharge cutoff voltage is 2.7 V. The input current, terminal voltage and processed SOC data are shown in Fig. 14(a) and (b).

Fig. 16(a) and (b) depicts the voltage prediction results in the CS2 battery. It is evident that the CS2 battery undergoes numerous charge and discharge cycles and operates under complex conditions. With the exception of the proposed method, the errors of the other three comparison methods are approximately 1 V, leading to less-than-ideal voltage fitting effects, especially when aging occurs. The voltage fitting image clearly shows that the proposed method can effectively track the voltage curve, with an error margin smaller than that of the other three methods. The statistical values presented in Table VI further highlight the comparison of effects. Specifically, the MAE and RMSE of the proposed method are 51.8 and 64.4 mV, respectively. Even under more complex aging conditions, this method maintains its stability.

### *B. The Experiment on $LiFePO_4$ Aged Battery*

The second experiment was carried out on 94Ah $\text{LiFePO}_4$ battery produced by a certain manufacturer. The relevant battery parameters are shown in Table V, and the power battery test system used is shown in Fig. 15. All aging data are aged by 1C constant current charge and discharge cycle at 52 °C until the battery capacity decays to less than 80% of the initial capacity. The input current, output voltage and processed SOC data in the experiment are shown in Fig. 14(c) and (d).

Fig. 16(c) and 16(d) shows the verification results of the four methods in $\text{LiFePO}_4$ battery. It can be seen that the voltage fitting effect of the four methods is ideal under relatively gentle working conditions, the effect of LTPV+ARPBSID is even better, and the voltage error is stably controlled within 0.005 V. Furthermore, the RLS method requires fewer initialization parameters, while the initial covariance matrices of the process and measurement errors in the JEKF and JUKF methods have a significant impact on the identification results, which leads to divergent prediction outcomes. The ARPBSID algorithm, which only contains three linear regression equations, has a simpler solution process, resulting in better fitting performance compared to the two aforementioned methods. The proposed method, based on RLS, incorporates an adaptive strategy for the forgetting factor, thus achieving higher accuracy and robustness in voltage tracking.

The statistical values in Table VI show the superiority of the proposed method. The MAE of LTPV+ARPBSID is about 13.6 mV, and the RMSE is 16.0 mV. The LTPV model has higher accuracy and stronger online prediction ability than the other three schemes. The proposed ARPBSID algorithm has better adaptability.

### *C. The Experiment on 18650-NCM Aged Battery*

The data for the third battery comes from the publicly available dataset released by Xi'an Jiaotong University [41]. This battery is manufactured by LISHEN and is a model 18650 nickel–cobalt–manganese (NCM) lithium-ion battery. The relevant battery parameters are shown in Table V. The battery's charge-discharge strategy is as follows: it is charged with a

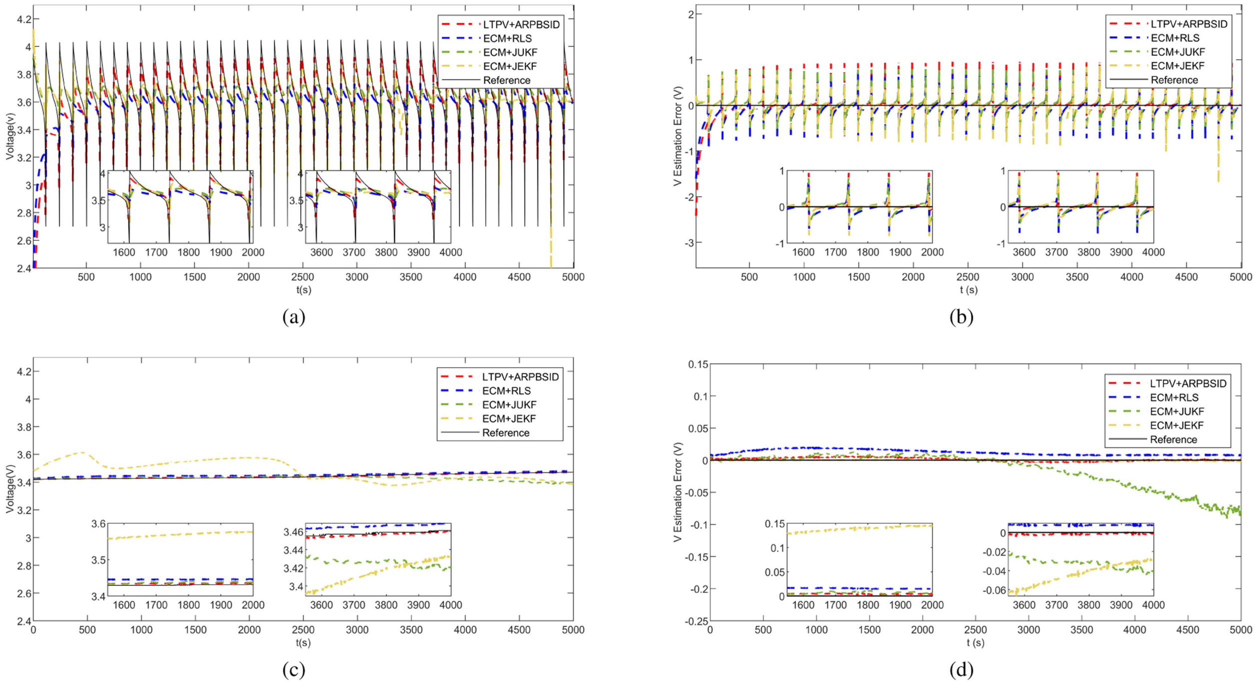

(a) (b)

(c) (d)

Fig. 16. Experimental result. (a) voltage estimation results in a CS2 battery. (b) Voltage estimation errors in CS2 battery. (c) Voltage estimation results in $LiFePO_4$ battery. (d) Voltage estimation errors in $LiFePO_4$ battery.

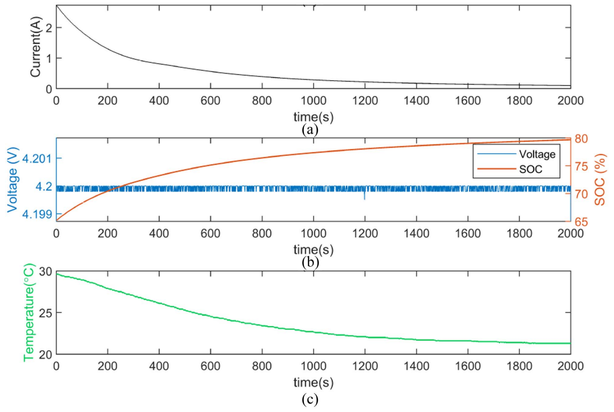

Fig. 17. Aged battery data details with temperature changes. (a) The input current in the 18650-NCM battery. (b) The output voltage and SOC in the 18650-NCM battery. (c) The temperature in the 18650-NCM battery.

constant current of 2 C until it reaches 4.2 V, then the voltage is held constant until the current drops to 0.05 C. After that, the battery rests for 5 min. Then, it is discharged with a constant current of 1 C until it reaches 2.5 V, followed by another 5-min rest. The data used in this section's experiment comes from the 2000 data points after the 299th cycle in batch 1 of the dataset. The data includes the variation in battery temperature during the experiment. The specific experimental data are shown in Fig. 17.

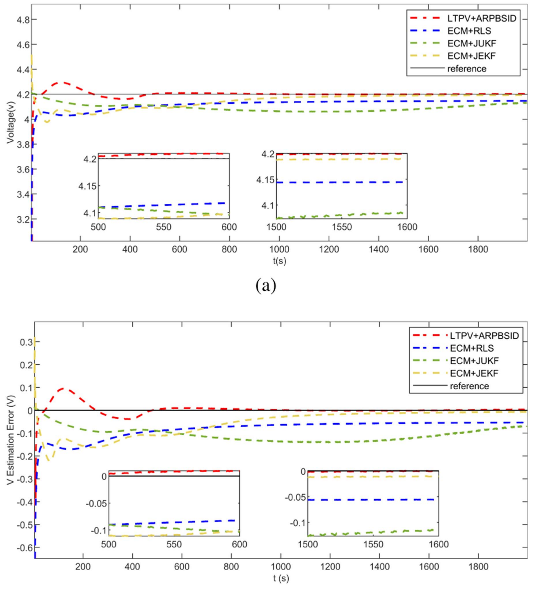

(a)

(b)

Fig. 18. Experimental result. (a) Voltage estimation results in 18650-NCM battery. (b) Voltage estimation errors in 18650-NCM battery.

The experimental results are shown in Fig. 18. The error of the LTPV+ARPBSID method is approximately 0.01 V, significantly outperforming the other three online algorithms. As further supported by the statistical data in Table VI, the proposed method also demonstrates excellent accuracy when the battery operates under varying temperature conditions.

## VI. CONCLUSION

Commonly used battery modeling methods often struggle to balance accuracy and simplicity. To address this challenge, this article introduces a general battery model architecture, LTPV model, with balance between the accuracy and complexity. The proposed model integrates internal and external factors that affect lithium batteries by a polynomial relationship. This approach extends the traditional ECM, preserving its simplicity while accommodating complex influencing factors. An online identification framework with three recursive least squares algorithms with adaptive forgetting factor is proposed to identify the LTPV model, which transforms the complex identification problem into the sequential solution of three unary linear problems, significantly simplifying the calculation process. The adaptive forgetting factor can address errors from aging effects and parameter changes and quickly adapt to rapid parameter changes. The effectiveness of the proposed algorithm is validated through simulations and real data from three different battery types. The proposed method is providing a foundational battery model for applications in specific control fields. However, our current research focus remains on the accurate modeling of lithium batteries only, mainly aimed at addressing issues such as parameter variations, aging, and degradation caused by external characteristics and internal reactions. Therefore, it is still in the developmental stage regarding subsequent research on controller design after modeling to deal time delays, and managing the power flow between the lithium battery system and the external grid [42], [43]. Furthermore, the performance of the lithium battery model under extreme temperatures and severe aging degradation conditions remains one of the challenges for this method, which we will continue to explore in future work.

## REFERENCES

[1] J. Ding, Y. Yang, and J. Yao, “Multi-innovation and strong tracking based hfilter for state of charge estimation of lithium-ion batteries,” *J. Energy Storage*, vol. 85, 2024, Art. no. 111039.

[2] Z. Deng, L. Yang, Y. Yang, Z. Wang, and P. Zhang, “Application of electrochemical model of a lithium-ion battery,” *Chem. Technol. Fuels Oils*, vol. 58, no. 3, pp. 519–529, 2022.

[3] N. Khosravi, M. Dowlatabadi, M. B. Abdelghany, M. Tostado-Véliz, and F. Jurado, “Enhancing battery management for hevs and evs: A hybrid approach for parameter identification and voltage estimation in lithium-ion battery models,” *Appl. Energy*, vol. 356, 2024, Art. no. 122364.

[4] M. Saeed, S. Lu, Z. Song, and X. Hu, “Integrated framework for accurate state estimation of lithium-ion batteries subject to measurement uncertainties,” *IEEE Trans. Power Electron.*, vol. 39, no. 7, pp. 8813–8823, Jul. 2024.

[5] Z. Li, Y. Yang, L. Li, and D. Wang, “A weighted pearson correlation coefficient based multi-fault comprehensive diagnosis for battery circuits,” *J. Energy Storage*, vol. 60, 2023, Art. no. 106584.

[6] K.-H. Kim, K.-H. Oh, H.-S. Ahn, and H.-D. Choi, “Time–frequency domain deep convolutional neural network for li-ion battery soc estimation,” *IEEE Trans. Power Electron.*, vol. 39, no. 1, pp. 125–134, Jan. 2024.

[7] Y. Xie, W. Li, X. Hu, C. Zou, F. Feng, and X. Tang, “Novel mesoscale electrothermal modeling for lithium-ion batteries,” *IEEE Trans. Power Electron.*, vol. 35, no. 3, pp. 2595–2614, Mar. 2020.

[8] X. Zhang, Y. Wang, and Z. Chen, “Soc-modified core temperature estimation of lithium-ion battery based on control-oriented electro-thermal model,” *IEEE Trans. Power Electron.*, vol. 38, no. 9, pp. 11642–11651, Sep. 2023.

[9] D. Wang, “Key-term separation based hierarchical gradient approach for nn based hammerstein battery model,” *Appl. Math. Lett.*, vol. 157, 2024, Art. no. 109207.

[10] F. Naseri, E. Schaltz, D.-I. Stroe, A. Gismero, and E. Farjah, “An enhanced equivalent circuit model with real-time parameter identification for battery state-of-charge estimation,” *IEEE Trans. Ind. Electron.*, vol. 69, no. 4, pp. 3743–3751, Apr. 2022.

[11] X. Du et al., “An information appraisal procedure: Endows reliable online parameter identification to lithium-ion battery model,” *IEEE Trans. Ind. Electron.*, vol. 69, no. 6, pp. 5889–5899, Jun. 2022.

[12] D. Li, Z. Zhang, P. Liu, Z. Wang, and L. Zhang, “Battery fault diagnosis for electric vehicles based on voltage abnormality by combining the long short-term memory neural network and the equivalent circuit model,” *IEEE Trans. Power Electron.*, vol. 36, no. 2, pp. 1303–1315, Feb. 2021.

[13] X. Liu, Y. Gao, K. Marma, Y. Miao, and L. Liu, “Advances in the study of techniques to determine the lithium-ion battery’s state of charge,” *Energies*, vol. 17, no. 7, 2024, Art. no. 1643.

[14] Z. Xi, M. Dahmardeh, B. Xia, Y. Fu, and C. Mi, “Learning of battery model bias for effective state of charge estimation of lithium-ion batteries,” *IEEE Trans. Veh. Technol.*, vol. 68, no. 9, pp. 8613–8628, Sep. 2019.

[15] K. Bellache, M. B. Camara, B. Dakyo, and S. Ramasamy, “Aging characterization of lithium iron phosphate batteries considering temperature and direct current undulations as degrading factors,” *IEEE Trans. Ind. Electron.*, vol. 68, no. 10, pp. 9696–9706, Oct. 2021.

[16] M. Elmahallawy, T. Elfouly, A. Alouani, and A. M. Massoud, “A comprehensive review of lithium-ion batteries modeling, and state of health and remaining useful lifetime prediction,” *IEEE Access*, vol. 10, pp. 119040–119070, 2022.

[17] D. J. Docimo and H. K. Fathy, “Analysis and control of charge and temperature imbalance within a lithium-ion battery pack,” *IEEE Trans. Control Syst. Technol.*, vol. 27, no. 4, pp. 1622–1635, Jul. 2019.

[18] J. Ren, J. Ma, H. Wang, T. Yu, and K. Wang, “A comprehensive review on research methods for lithium-ion battery of state of health estimation and end of life prediction: Methods, properties, and prospects,” *Protection Control Modern Power Syst.*, pp. 1–20, 2024.

[19] Z. Yu, R. Huai, and H. Li, “Cpso-based parameter-identification method for the fractional-order modeling of lithium-ion batteries,” *IEEE Trans. Power Electron.*, vol. 36, no. 10, pp. 11109–11123, Oct. 2021.

[20] R. Xiong, L. Li, Q. Yu, Q. Jin, and R. Yang, “A set membership theory based parameter and state of charge co-estimation method for all-climate batteries,” *J. Cleaner Prod.*, vol. 249, 2020, Art. no. 119380.

[21] S. Surya, A. Samanta, V. Marcis, and S. Williamson, “Hybrid electrical circuit model and deep learning-based core temperature estimation of lithium-ion battery cell,” *IEEE Trans. Transport. Electrific.*, vol. 8, no. 3, pp. 3816–3824, Sep. 2022.

[22] Y. Zheng, W. Gao, X. Han, M. Ouyang, L. Lu, and D. Guo, “An accurate parameters extraction method for a novel on-board battery model considering electrochemical properties,” *J. Energy Storage*, vol. 24, 2019, Art. no. 100745.

[23] W. D. Widanage et al., “Design and use of multisine signals for li-ion battery equivalent circuit modelling. part 2: Model estimation,” *J. Power Sources*, vol. 324, pp. 61–69, 2016.

[24] H. Beelen, H. J. Bergveld, and M. Donkers, “Joint estimation of battery parameters and state of charge using an extended kalman filter: A single-parameter tuning approach,” *IEEE Trans. Control Syst. Technol.*, vol. 29, no. 3, pp. 1087–1101, May 2021.

[25] Y. Wang, C. Zhang, and Z. Chen, “A method for joint estimation of state-of-charge and available energy of $LiFePO_4$ batteries,” *Appl. Energy*, vol. 135, pp. 81–87, 2014.

[26] S. Zhang, X. Wang, Z. Chen, and D. Xiao, “Anti-disturbance state-of-charge estimation for lithium-ion batteries using nonlinear extended state observers,” *IEEE Trans. Transport. Electrific.*, vol. 11, no. 1, pp. 2918–2928, Feb. 2025.

[27] Y. Hu and S. Yurkovich, “Battery cell state-of-charge estimation using linear parameter varying system techniques,” *J. Power Sources*, vol. 198, pp. 338–350, 2012.

[28] F. Hoekstra, M. Donkers, and H. Bergveld, “Rapid empirical battery electromotive-force and overpotential modelling using input–output linear parameter-varying methods,” *J. Energy Storage*, vol. 65, 2023, Art. no. 107185.

[29] J. Hou, H. Su, C. Yu, F. Chen, and P. Li, “Bias-correction errors-in-variables hammerstein model identification,” *IEEE Trans. Ind. Electron.*, vol. 70, no. 7, pp. 7268–7279, Jul. 2023.

[30] J. Hou, F. Chen, P. Li, and Z. Zhu, “Gray-box parsimonious subspace identification of Hammerstein-type systems,” *IEEE Trans. Ind. Electron.*, vol. 68, no. 10, pp. 9941–9951, Oct. 2021.

[31] G. Mercère, L. Bako, and S. Lecœuche, “Propagator-based methods for recursive subspace model identification,” *Signal Process.*, vol. 88, no. 3, pp. 468–491, 2008.

[32] J. Munier and G. Y. Delisle, “Spatial analysis using new properties of the cross-spectral matrix,” *IEEE Trans. Signal Process.*, vol. 39, no. 3, pp. 746–749, Mar. 1991.

[33] Z. Wei, C. Zou, F. Leng, B. H. Soong, and K.-J. Tseng, “Online model identification and state-of-charge estimate for lithium-ion battery with a recursive total least squares-based observer,” *IEEE Trans. Ind. Electron.*, vol. 65, no. 2, pp. 1336–1346, Feb. 2018.

[34] J. Hou et al., “Robust lithium-ion state-of-charge and battery parameters joint estimation based on an enhanced adaptive unscented kalman filter,” *Energy*, vol. 271, 2023, Art. no. 126998.

[35] Z. Wei, G. Dong, X. Zhang, J. Pou, Z. Quan, and H. He, “Noise-immune model identification and state-of-charge estimation for lithium-ion battery using bilinear parameterization,” *IEEE Trans. Ind. Electron.*, vol. 68, no. 1, pp. 312–323, Jan. 2021.

[36] N. Omar et al., “Lithium iron phosphate based battery–assessment of the aging parameters and development of cycle life model,” *Appl. Energy*, vol. 113, pp. 1575–1585, 2014.

[37] L. Sun, G. Li, and F. You, “Combined internal resistance and state-of-charge estimation of lithium-ion battery based on extended state observer,” *Renewable Sustain. Energy Rev.*, vol. 131, 2020, Art. no. 109994.

[38] J. Zhu et al., “An improved electro-thermal battery model complemented by current dependent parameters for vehicular low temperature application,” *Appl. Energy*, vol. 248, pp. 149–161, 2019.

[39] Y. Li, L. Wang, Y. Feng, C. Liao, and J. Yang, “An online state-of-health estimation method for lithium-ion battery based on linear parameter-varying modeling framework,” *Energy*, vol. 298, 2024, Art. no. 131277.

[40] U. U. o. M. Group CBR, “CALCE center for advanced life cycle engineering lithium-ion battery experimental data,” College Park, MD, USA, 2015, [Online]. Avaliable: https://calce.umd.edu/data

[41] F. Wang, Z. Zhai, Z. Zhao, Y. Di, and X. Chen, “Physics-informed neural network for lithium-ion battery degradation stable modeling and prognosis,” *Nature Commun.*, vol. 15, no. 1, 2024, Art. no. 4332.

[42] M. B. Abdelghany, A. Al-Durra, H. H. Zeineldin, and F. Gao, “A coordinated multitimescale model predictive control for output power smoothing in hybrid microgrid incorporating hydrogen energy storage,” *IEEE Trans. Ind. Informat.*, vol. 20, no. 9, pp. 10987–11001, Sep. 2024.

[43] S. E. Sati et al., “Economic power-sharing and stability enhancement for virtual synchronous generators in islanded mg,” *IEEE Trans. Power Syst.*, vol. 40, no. 1, pp. 188–203, Jan. 2025.

**Jie Hou** (Member, IEEE) received the B.Eng. degree in automation from North Minzu Uni-versity, Yinchuan, China, in 2010, the M.Eng. degree in control science and engineering from Chongqing University, Chongqing, China, in 2013, and the Ph.D. degree in control theory and control engineering from the Dalian University of Technology, Dalian, China, in 2018.

From 2018 to 2021, he was a Lecturer with the Chongqing University of Posts and Telecommunications, Chongqing, where he is currently an Associate Professor. His current research interests include system identification and modeling

**Yuchao Jiang** received the B.S. degree in automation from Chongqing University of Science & Technology, Chongqing, China, in 2022, and the M.S. degree in control engineering from the Chongqing University of Posts and Telecommunications, Chongqing, China, in 2024.

Her research interests covers identification and modeling.

**Jingxiang Liu** (Member, IEEE) received the Ph.D. degree in control theory and control engineering from the School of Control Science and Engineering, Dalian University of Technology, Dalian, China, in 2019.

He is currently an Associate Professor with the College of Marine Electrical Engineering, Dalian Maritime University, Dalian, China. His research interests include intelligent monitoring for complex industrial processes, digital modeling for complex systems, machine learning and deep learning research and application.

**Penghua Li** (Member, IEEE) received the B.S. degree in electronic information science and technology and the Ph.D. degree in control theory and engineering both from Chongqing University, China, in 2008 and 2012, respectively.

He is currently a Professor with the Chongqing University of Posts and Telecommunications. His current research interests include image recognition and speech recognition.

**Sheng Xiang** (Member, IEEE) received the B.Eng. degree in mechanical engineering from Yangtze University, Hubei, China, in 2017, and the Ph.D. degree in mechanical engineering from Chongqing University, Chongqing, China, in 2022.

He is currently a Lecturer with the Chongqing University of Posts and Telecommunications. His current research interests include fault diagnosis and prognosis.

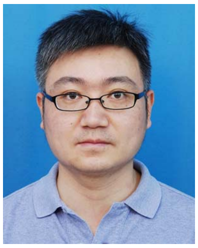

**Liping Chen** (Member, IEEE) received the B.S. degree in applied mathematics from Anhui Normal University, Wuhu, China, in 2007, the M.S. degree in basic mathematics from Anhui University, Hefei, China, in 2010, and the Ph.D. degree in control theory and engineering from the School of Automation, Chongqing University, Chongqing, China, in 2013.

He is currently a Professor with Hefei University of Technology. His current research interests include the states estimation and health diagnosis of lithiumion batteries, fractional-order systems, and nonlinear dynamical systems.

**Zhongwei Deng** (Senior Member, IEEE) received his Ph.D. in mechanical engineering from the Shanghai Jiao Tong University, Shanghai, China, in 2019. He previously finished his B.S. from Jilin University, China, in 2014. He was an Assistant/Postdoctoral Researcher in the College of Mechanical and Vehicle Engineering, Chongqing University, China, from 2019–2022. He is currently an Associate Professor in the School of Mechanical and Electrical Engineering, University of Electronic Science and Technology of China, China. He is also a Visiting Scholar in the ISEA, RWTH Aachen University, Germany. His research interests focus on data-driven and electrochemical mechanism modeling, parameter identification, states estimation, health management, fault diagnosis, and second-life utilization of lithium-ion batteries.